

# Anisotropic diffusion creep in post-perovskite provides a new model for deformation at the core-mantle boundary.

David P Dobson<sup>1,2</sup> Alexander Lindsay-Scott<sup>1</sup> Simon A Hunt<sup>1</sup>, Edward Bailey<sup>1,3</sup>, Ian G Wood<sup>1</sup>, John P Brodholt<sup>1,4</sup>, Lidunka Vocadlo<sup>1</sup>, and John Wheeler<sup>5</sup>.

1. Department of Earth Sciences, University College London, Gower Street, London WC1E 6BT, UK.
2. Bayerisches Geoinstitut, Universität Bayreuth, D-95440 Bayreuth, Germany.
3. Now at: Department of Chemical Engineering, Imperial College London, SW7 2AZ, UK.
4. Centre for Earth Evolution and Dynamics (CEED), University of Oslo, 0316 Oslo, Norway
5. Department of Earth, Ocean and Ecological Sciences, University of Liverpool, UK, L69 3GP.

## Abstract

The lowermost portion of Earth's mantle ( $D''$ ) above the core-mantle boundary shows anomalous seismic features, such as strong seismic anisotropy, related to the properties of the main mineral  $\text{MgSiO}_3$  post-perovskite. But, after over a decade of investigations, the seismic observations still cannot be explained simply by flow models which assume dislocation creep in post-perovskite. We have investigated the chemical diffusivity of perovskite and post-perovskite phases by experiment and *ab initio* simulation, and derive equations for the observed anisotropic diffusion creep. There is excellent agreement between experiments and simulations for both phases in all the chemical systems studied. Single-crystal diffusivity in post-perovskite displays at least 3 orders of magnitude of anisotropy by experiment and simulation ( $D_a = 1000 D_b$ ;  $D_b \approx D_c$ ) in zinc-fluoride and an even more extreme anisotropy is predicted ( $D_a = 10000 D_c$ ;  $D_c = 10000 D_b$ ) in the natural  $\text{MgSiO}_3$  system. Anisotropic chemical diffusivity results in anisotropic diffusion-creep, texture generation and a strain weakening rheology. The results for  $\text{MgSiO}_3$  post-perovskite strongly imply that regions within the  $D''$  region of the Earth dominated by post-perovskite will (1) be substantially weaker than regions dominated by perovskite and (2) develop a strain-induced crystallographic-preferred orientation with strain-weakening rheology. This leads to strain localisation and the possibility to bring regions with significantly varying textures into close proximity by strain on narrow shear zones. Anisotropic diffusion creep therefore provides an attractive alternative explanation for the complexity in observed seismic anisotropy and the rapid lateral changes in seismic velocities in  $D''$ .

## Significance Statement

The Earth's core-mantle region is an important, but poorly understood, region which drives mantle convection (and hence surface processes) by heat transfer from the core to the mantle. Seismic observations show the complexity of the region but current geodynamic modelling of lowermost mantle flow is hindered by an incomplete understanding of the rheology of the main mineral, post-perovskite. Here we show that post-perovskite is strongly anisotropic in diffusion creep and hence will show non-linear behaviours during deformation, including strain weakening and localization.

This will help to explain much of the observed seismic complexity of the core-mantle boundary region.

## Main Text

The post-perovskite phase (CaIrO<sub>3</sub>-type) of (Mg,Fe)(Si,Al)O<sub>3</sub> is stable at pressures above ~120 GPa<sup>1-3</sup>, corresponding to the D'' region of Earth's lowermost mantle. Its strongly anisotropic elastic and rheological properties have been invoked to explain observations of strong seismic anisotropy in D'' which are interpreted as requiring creep by a dislocation migration process. If we can determine the active flow mechanisms of post-perovskite this then offers the possibility of interpreting the D'' seismic anisotropy in terms of convective patterns deep in the Earth, and using them to map flow further back into deep time than current plate reconstructions allow<sup>4-7</sup>. This has important implications for understanding many first order questions about the deep Earth, such as the degree of mixing, the ultimate fate of slabs as well as the longevity of seismic anomalies such as LLSVPs.

In order to interpret the seismic observations, one must fully understand the relationships between strain and texture generation in mantle rocks. Although there have been many studies attempting to do this for post-perovskite<sup>8-16</sup>, no unique solution has been found which fits the globally observed seismic anisotropy using a single slip system in post-perovskite (e.g.; ref.15). In particular strong changes in anisotropy observed around hot regions of D'' are difficult to explain by simple flow and dislocation creep. One aspect that has been relatively ignored is the remarkably large anisotropy in diffusion rates along different crystallographic directions predicted in *ab initio* calculations, with up to 8 orders of magnitude difference between the fast and slow diffusion directions in post-perovskite<sup>17</sup>. This would be the largest diffusion anisotropy seen in any material, to the best of our knowledge, and if correct might have significant implications for the dynamics of the core-mantle boundary region. However, there have not as yet been any studies to test whether the predicted diffusion anisotropy is real. Furthermore, only one study has investigated the effect of the anisotropic diffusion on the rheology of D''<sup>18</sup> and only for deformation by either pure dislocation glide or climb-assisted glide. And crucially, there have been no studies to date of the effect of extreme anisotropic diffusion on lattice-diffusion creep. This is because the observation of seismic anisotropy is generally thought to require dislocation creep. However, the high temperatures and low stresses of the core-mantle boundary, combined with the very small grain size expected in post-perovskite<sup>12,19</sup>, would argue for diffusion creep to be the active deformation mechanism in D''. Here we present a combined *ab initio* simulation and multi-anvil experimental study of chemical diffusion in both the perovskite and post-perovskite structures in a fluoride analogue system. Fluorides have been shown to be a good analogue for the silicate system with similar crystal chemistry in both perovskite and post-perovskite structures (ref 20 and references therein) and transforming via the same martensitic-like mechanism between the two phases<sup>12</sup>. We find that similar to the silicate system, the fluoride system also displays extreme anisotropy in chemical diffusivity in the post-perovskite phase. By developing an analytical solution for strain in grains with anisotropic chemical diffusivities we show that diffusion anisotropy will create a strain weakening rheology, with the ultimate strain rate controlled by the fastest diffusion direction. We observe that the crystallographically-controlled shape anisotropy of crystals deforming in lattice-diffusion creep leads to crystallographic-preferred orientation in crystals deforming by lattice-diffusion creep and discuss the implications of anisotropic diffusion creep for the D'' region.

We prepared diffusion-couples of  $\text{NaZnF}_3 - \text{NaXF}_3$  ( $X = \text{Mn, Co, Fe}$ ) from pre-sintered and polished pure end-member perovskite samples and annealed them at pressures ranging from  $\sim 2$  to 14 GPa and temperatures from 823 to 1073 K (see SI Appendix, section S1 for details). Recovered samples were analysed by energy-dispersive EPMA for Zn-X concentration gradient and a Boltzmann-Matano analysis was applied to the observed diffusion profiles. The zinc diffusivities extrapolated to pure  $\text{NaZnF}_3$  composition (equivalent to zinc-self diffusivity) are presented in figure 1. The perovskite-diffusion coefficients at 10 GPa and below are well fitted by the Arrhenius relation,

$$D = D_0 e^{-\frac{\Delta H + P\Delta V}{RT}} \quad 1,$$

with parameters:  $\ln D_0 = 13.4 \pm 9.2 \text{ cm}^2\text{s}^{-1}$ ;  $\Delta H = 317 \pm 74 \text{ kJmol}^{-1}$ ;  $\Delta V = 5.5 \pm 1.4 \text{ cm}^3$ . The 14 GPa perovskite datum falls significantly above the predicted value from the Arrhenius fit, however this sample transformed to post-perovskite during the experiment, which means that its final measured diffusivity falls between that of perovskite and post-perovskite. Pre-synthesised post-perovskite has a bulk chemical diffusivity at 14 GPa substantially larger than the predicted value for perovskite at 14 GPa and with a much smaller activation enthalpy ( $88 \pm 15 \text{ kJmol}^{-1}$ , based on two measurements; the end-member values of the Boltzmann-Matano fits to all experiments are presented in SI Appendix, Table S1). The increased chemical diffusivity in post-perovskite is also seen in the *ab initio* simulations of  $\text{NaZnF}_3$  post-perovskite which predict a difference in bulk Zn-diffusivity between perovskite and post-perovskite of 2.8 orders of magnitude at 14 GPa and 1073 K (Figure 2). Direct comparison of the predicted *ab initio* vacancy diffusivities with the experimental results requires knowledge of the vacancy concentration, which is not trivial for transition-metal-bearing systems. A concentration of 3.5 ppm zinc vacancies per formula unit, brings the experimental results into excellent agreement with the simulations for both phases. The simulated Schottky vacancy formation energies per atom at 14 GPa and resultant intrinsic Zn-vacancy concentrations are respectively 180 kJ/mole and 5 ppb for perovskite, and 170 kJ/mole and 13 ppb for post-perovskite. It seems reasonable, therefore, that the defect population is dominated by extrinsic vacancies under the experimental conditions. Regardless of whether the value of 3.5 ppm for the extrinsic vacancy concentration is the correct value, the ratio of zinc diffusivities in perovskite and post-perovskite shows excellent agreement between the experiments and simulations.

The  $\text{NaZnF}_3$  post-perovskite simulations show a large anisotropy, with diffusion in the  $\langle 100 \rangle$  direction 4.5 orders of magnitude faster than diffusion in the slowest,  $\langle 010 \rangle$ , direction. This sense of anisotropy is that same as predicted for  $\text{MgSiO}_3$  perovskite<sup>17</sup> and the 6-hop cycle previously found in the computer simulations to be faster than direct diffusion in the  $\langle 010 \rangle$  direction also dominates here for  $\langle 010 \rangle$ . While the experimental measured bulk diffusivity in post-perovskite agrees well with the bulk average of the predicted single-crystal values it is necessary to compare the simulations with experimental single-crystal measurements to confirm the predicted anisotropy.

Figure 3 shows a single crystal of  $\text{NaCoF}_3$  post-perovskite embedded in finely crystalline  $\text{NaZnF}_3$  from a diffusion experiment at 14 GPa and 823 K. The fluoride post-perovskites form with rod- or needle-habits (with aspect ratios ranging from 4:1 for  $\text{CaIrO}_3$  to  $>10:1$  for  $\text{NaNiF}_3$ ) with their a-axis parallel to the rod/needle axis<sup>20-22</sup>. The observed diffusion profile in the direction of the long axis of the crystal is well fitted with a Co-diffusivity in the single crystal of  $5.3 \pm 0.42 \times 10^{-14} \text{ cm}^2/\text{s}$  and a matrix Zn-diffusivity of  $2.0 \pm 1.0 \times 10^{-14} \text{ cm}^2/\text{s}$  (figure 3 b). The radial (ie perpendicular to the long axis of the crystal) diffusivity is substantially smaller, with a diffusion profile length which is similar to the

analytical spot size (figure 3 c). In this case, the beam convolution is significant to the fit – the dashed line in figure 3 c is the best-fitting diffusion profile and the solid line is this diffusion profile convolved with a Gaussian beam correction<sup>23</sup> with a standard deviation of 0.35  $\mu\text{m}$ . The effect of the beam convolution in the axial direction is so small that the two lines are indistinguishable in figure 3 b. The measured radial diffusivities are  $6.1 \pm 3.4 \times 10^{-17} \text{ cm}^2/\text{s}$  and  $7.1 \pm 2.2 \times 10^{-15} \text{ cm}^2/\text{s}$  respectively for the cobalt in the crystal and zinc in the matrix, giving an observed anisotropy for this crystal of three orders of magnitude for the single crystal but a reasonable agreement for the matrix diffusivity measured in the axial and radial directions. Multiple measurements give mean single-crystal Co-diffusivities in the axial and radial directions of  $5.5 \pm 0.3 \times 10^{-14} \text{ cm}^2/\text{s}$  and  $3.7 \pm 1 \times 10^{-17} \text{ cm}^2/\text{s}$  respectively, and a Zn-diffusivity of  $8.2 \pm 1 \times 10^{-15} \text{ cm}^2/\text{s}$  in the matrix. We therefore observe an apparent anisotropy in  $\text{NaCoF}_3$  post-perovskite of 3 orders of magnitude at 823 K but we consider this to be a minimum anisotropy as our errors are likely to cause an overestimate of the diffusivity in the radial direction (see SI Appendix, section S1.5). The inability to determine the crystal orientation in the diffusion couple, due to the small crystal size and weak metastability of fluoride post-perovskite means we are limited to comparing the axial value with the mean radial value. The long axis of post-perovskite crystals is invariably the a-axis in a range of systems<sup>11,20-22</sup>, but we cannot identify the orientation of the other two axes in our diffusion couple. The observed radial diffusivity displays the most variability in the experiments; if we assume that this arises from differences in the diffusivities in the b- and c- axial directions then, by comparison with the simulations we can ascribe the smallest and largest radial diffusivities to the b and c directions respectively. This would give  $D_a = 5.6 \pm 0.3 \times 10^{-14} \text{ cm}^2/\text{s}$ ,  $D_b = 4.6 \pm 1.2 \times 10^{-18} \text{ cm}^2/\text{s}$ ,  $D_c = 1.7 \pm 1.3 \times 10^{-16} \text{ cm}^2/\text{s}$  or 4 orders of magnitude difference between the fastest and slowest directions, in reasonable agreement with *ab initio*-predicted value of 4.5 orders of magnitude. We stress here that these experiments are likely to provide minimum estimates of the anisotropy in single-crystal post-perovskite diffusion.

In addition to the close agreement between experiment and simulations in the fluoride system studies, we have also found close agreement between (*ab initio*) predictions and experimental measurements of anisotropy in  $\text{CaIrO}_3$  post-perovskite single crystals for Pt-Ir interdiffusion<sup>24</sup>, however the total anisotropy in this system was only  $D_a \approx 4D_b$  necessitating the present study to confirm the extreme anisotropy predicted for the silicate system. It is therefore clear that the *ab initio* simulations do correctly predict the anisotropy across a range of post-perovskite analogues with widely varying anisotropies, as well as the absolute values for relevant systems (fluoride perovskite and post-perovskite,  $\text{MgSiO}_3$ -perovskite<sup>17</sup>,  $(\text{Mg,Fe})\text{O}$  ref.<sup>17</sup>) which have been measured experimentally. This sense of anisotropy, can be explained by the same crystal chemical arguments as explains the more moderate anisotropy in olivine and feldspars, and the extreme values of anisotropy are largely explicable by the effect of the pressure acting on the activation volume of the diffusion in the different directions (see SI Appendix, section S2) . We are therefore confident that the anisotropy of chemical diffusivity from the simulations in silicate post-perovskite<sup>17</sup>, with  $D_a \approx 10^4 D_c \approx 10^8 D_b$ , is correct and we now explore some consequences of extreme anisotropic chemical diffusivity for diffusion-creep deformation of post-perovskite in  $D''$ .

First, we reiterate that shape anisotropy is seen in all low-pressure analogue post-perovskite-structured materials<sup>20-22,25</sup> (and related structures such as stibnite,  $\text{Sb}_2\text{S}_3$ ) and suggest that magnesium-silicate post-perovskite will also grow with a [100]-rod morphology. This is consistent with post-perovskite morphologies which would be predicted from growth morphology theories

based on lattice spacings<sup>26-28</sup> or attachment energies<sup>29</sup>. Anisotropic crystal shapes result in anisotropic rheology for deformation by diffusion creep of the form  $\dot{\epsilon}_i \propto D/X_i^2$ , where  $\dot{\epsilon}_i$  is the strain rate and  $X_i$  is the length of the crystal in the  $i$ th direction (SI Appendix, section 3). This shape-controlled creep anisotropy can be modified during the rotation of grains which is required by diffusion creep. Grain rotation during deformation tends to break up needles and rods by microboudinage leading to deformation-induced reduction of grain-shape anisotropy of needles<sup>30</sup>. The processes which cause this boudinage vary depending on strain rate and temperature<sup>31</sup>, but at least some of them can operate in the diffusion creep regime<sup>30,32</sup>, and can be accompanied by other processes which reduce grain size during crystal stretching in diffusion creep<sup>32</sup>. In general, this will result in a reduction in diffusion-creep strength by needle breaking and a reduction in the aspect ratio of needles, as has been seen in some industrial materials<sup>33</sup>, but in post-perovskite shape anisotropy does not operate in isolation and the extreme anisotropy of chemical diffusivity must also be considered.

We derive an analytical solution for the case of rectangular grains oriented with their crystallographic axes normal to crystal faces and explore various scenarios in the SI Appendix, section 3. Strain rates in each direction are strongly influenced by  $D_i/X_i^2$  where  $i$  denotes the  $i$ th

direction and  $X$  is the dimension in that direction. For anisotropies where one diffusing direction is much slower than the other two directions, as in post perovskite ( $D_a, D_c \gg D_b$ ) there is no significant strain in the slow direction for any reasonable values of stress and strain is confined to the X-Z plane. However, the relative strain rates in the other two directions are a complex interplay between the chemical diffusivities and crystal dimensions in those directions. The evolution of a grain of MgSiO<sub>3</sub> post-perovskite, with initial dimensions of 1 mm x 1 mm x 1 mm, under core-mantle boundary conditions and an applied differential stress of 5 MPa is presented in figure 4. The figure shows that it is easy to stretch equant grains parallel to the a-axial direction and shrink them in the c-axial direction, but difficult to do the stretch along c. Thus, beginning with a random CPO, we predict the preferential development of bladed needles with the long axis parallel to a. Strain rates for extension parallel to X, parallel to the fast diffusing axial direction, are up to 500 times higher than for shortening parallel to X. Extension parallel to X also produces strain weakening by a factor of 50 after the first ~50Ma, whilst shortening just induces gradual strengthening. Both these observations are a consequence of the strain being initially rate limited by  $D_c/Z^2$ ; for stretching along X the crystal is shrinking in the Z-dimension whereas for compressions along X, Z must increase to conserve volume. However, once X is sufficiently large the strain becomes rate limited by  $D_a/X^2$ , and with continued strain the strain rate decreases. Taken at face value, this would suggest that the strain weakening is transient but, as discussed above, large shape anisotropies tend to be unstable against shear, with boudinage processes limiting the aspect ratio of grains. The maximum strain rate for the scenario shown in figure 4 occurs when  $X = 11$  mm,  $Y = 1$  mm and  $Z = 90$   $\mu$ m which, with an aspect ratio of over 100:1 will be susceptible to boudinage and hence grain-size (and aspect ratio) reduction. We therefore suggest that ongoing deformation will result in continued strain weakening by stretching along X accompanied by repeated boudinage.

We have shown that the extreme anisotropy of diffusivity in post-perovskite should result in strain-weakening rheology. In addition to strain weakening, the formation of bladed needles of the form

shown in figure 4 will result in development of a shape preferred orientation since anisotropic grains undergoing shear settle with their long axes parallel to elongation and their intermediate axes perpendicular to the shear profile plane as shown in numerical models of anisotropic ellipsoids under shear strain (see SI Appendix, sections S4 and S5). Since the shape anisotropy is a result of diffusion anisotropy this also implies CPO formation with a-axes oriented parallel to the stretching direction and b-axes perpendicular to the shear-profile plane. There are several experimental studies which show that the generation of CPO is possible during diffusion-creep deformation of olivine<sup>34,35</sup> and anorthite<sup>36</sup>. Here we show that, in addition to those examples of texture generation in diffusion-creep, anisotropic chemical diffusivity should in itself generate texture by formation of strongly anisotropic crystal shapes. Development of CPO in mica has been observed in micaceous metapelites accompanied by preferential diffusion creep along the fast diffusion direction (in that case diffusion within the mica (001) plane is  $\sim 4$  orders of magnitude faster than diffusion perpendicular to this plane)<sup>37</sup>. For  $\text{MgSiO}_3$  post-perovskite deforming by diffusion creep in a horizontal flow field along the core-mantle boundary texture will develop with a-axes oriented parallel to the flow direction with c-axes oriented vertically.

As dislocation creep is generally thought to be a requirement to produce CPO, the observation of seismic anisotropy in  $D''$  has led to the common assumption that dislocation-creep must dominate deformation in  $D''$ . However, our results show that anisotropic diffusion creep in post-perovskite is also able to produce CPO, and as discussed earlier, diffusion creep is in fact more consistent with the strain rates and stress expected in the  $D''$  region<sup>38</sup> and the likely grain size of post-perovskite (SI Appendix, section 6). An anisotropic diffusion-creep controlled deformation mechanism of the form described here has a number of fundamental implications for the Earth's lowermost mantle. The first is that post-perovskite will be much weaker than perovskite, even when cooler. This is because post-perovskite deforming by diffusion creep will be controlled predominantly by the fastest diffusing direction. This is also consistent with recent atomistic simulations which show that post-perovskite deforming by dislocation creep will also be weak<sup>14</sup>, so regardless of which deformation mechanism is operating this finding is robust. Weak post-perovskite means that cool subducting slabs in  $D''$  will be weaker than warmer perovskite-bearing LLSVP regions, making LLSVPs more resistant to being deformed or pushed about by slabs. Secondly, the anisotropy formed by diffusion creep will not have the same dependence on strain as dislocation creep, and so mapping mantle flow from anisotropy with diffusion creep will produce a different flow pattern than flow models previously based on dislocation creep. The third implication is that post-perovskite deforming by diffusion creep in  $D''$  will exhibit a strain-weakening rheology. Strain weakening results in localization of deformation onto shear zones<sup>39</sup>. This is observed on all length scales in both brittle and plastic deformation, and is a key to generating plate-tectonic style convection in the Earth<sup>39</sup>. We suggest that a similar process might operate in the  $D''$  region resulting in strain being localised in narrow shear zones of strongly textured post-perovskite with larger regions between these shear zones suffering relatively little deformation. This will allow previously developed textures to survive in the non-deforming regions, something that would be very problematic when mapping seismic anisotropy onto mantle flow. Also rapid changes in observed seismic wave-speed<sup>40</sup> which are currently interpreted as compositional variations might simply be due to adjacent regions of very different anisotropy brought into close proximity along shear zones. In addition, shear zones which display a substantially different seismic anisotropy from their surroundings might contribute to scattering in the lowermost mantle. The development of shear zones within post-perovskite

dominated regions might also contribute to the long-term survival of the large-low-shear-velocity regions by localisation of strain to their outermost margins. Strong localisation of strain may also have a strong effect on heat flow in D'' due to the anisotropic thermal conductivity of post-perovskite<sup>41,42</sup>. If, as we argue, post-perovskite dominated regions of D'' are in fact deforming by diffusion creep, texture generation and strain localisation are likely to exert strong controls on the dynamics of D''. These processes should therefore be considered in future geodynamical and seismic studies of this region.

### Data Availability Statement

All data discussed in the paper will be made available to readers.

### Acknowledgments

This work was funded by NERC grants NE/L006898 and NE/L007363, and a Friedrich Wilhelm Bessel Research Award of the Alexander von Humboldt Stiftung to DPD. We thank Florian Heidelbach for assistance with SEM analyses.

### References

- 1 Murakami, M., Hirose, K., Kawamura, K., Sata, N., Ohishi, Y. Post Perovskite Phase Transition in MgSiO<sub>3</sub>. *Science*, 304, 855-858 (2004).
- 2 Oganov, A.R. & Ono S. Theoretical and Experimental Evidence for a Post-Perovskite Phase of MgSiO<sub>3</sub> in Earth's D'' layer. *Nature*, 430, 445-448 (2004).
- 3 Tsuchiya T, Tsuchiya J, Umemoto K, and Wentzcovitch RM. Phase transition in MgSiO<sub>3</sub> perovskite in the Earth's lower mantle. *Earth Planet. Sci. Lett.* 224, 241–248 (2004).
- 4 Wookey, J., and J.M. Kendall, Constraints on lowermost mantle mineralogy and fabric beneath Siberia from seismic anisotropy, *Earth Planet. Sci. Lett.*, 275, 32-42 (2008).
- 5 Merkel, S., A.K. McNamara, A. Kubo, S. Speziale, L. Miyagi, Y. Meng, T.S. Duffy, and H.R. Wenk, Deformation of (Mg,Fe) SiO<sub>3</sub> post-perovskite and D anisotropy, *Science*, 316, 1729-1732 (2007).
- 6 Walker, A. M., A. M. Forte, J. Wookey, A. Nowacki, and J.-M. Kendall. Elastic anisotropy of D'' predicted from global models of mantle flow, *Geochem. Geophys. Geosyst.*, 12, Q10006 (2011).
- 7 Wenk, H-R., Cottaar, S., Tomé, CN., McNamara, A. and Romanowicz, B. Deformation in the lowermost mantle: From polycrystal plasticity to seismic anisotropy. *Earth Planet. Sci. Lett.* 306, 33–45 (2011).
- 8 Merkel, S., McNamara, .K, Kubo, A., Speziale, S., Miyagi, L., Meng, Y., Duffy, TS. and Wenk, H-R. Deformation of (Mg,Fe)SiO<sub>3</sub> Post-Perovskite and D'' Anisotropy. *Science*, 316, 1729-1732 (2007).
- 9 Miyagi, L., Kanitpanyacharoen, W., Kaercher, P., Lee, KKM. and Wenk H-R. Slip Systems in MgSiO<sub>3</sub> Post-Perovskite: Implications for D'' Anisotropy. *Science* 329, 1639-1641 (2010).

- 10 Merkel, S., Kubo, A., Miyagi, L., Speziale, S., Duffy, T.S., Mao, H.-K. and Wenk, H.-K. Plastic Deformation of MgGeO<sub>3</sub> Post-Perovskite at Lower Mantle Pressures. *Science* 311, 644-646, (2006).
- 11 McCormack, R. J., Dobson, D.P., Walte, N., Miyajima, N. and Taniguchi, T. The development of shape- and crystallographic-preferred orientation in CaPtO<sub>3</sub> post-perovskite deformed in pure shear. *Amer. Mineral.*, 96, 1630-1636 (2011).
- 12 Dobson, D. P., Miyajima, N., Nestola, F., Alvaro, M., Casati, N., Liebske, C., Wood, I. G. and Walker, A. M. Inherited textures during the perovskite to post-perovskite transition and seismic anisotropy in D". *Nature Geosci.*, 6, 575-578 (2013).
- 13 Hunt, S.A., Weidner, D.J., Li, L., Wang, L., Walte, N.P. Brodholt, J.P. and Dobson, D.P., Weakening of CaIrO<sub>3</sub> during the perovskite-post perovskite transformation. *Nature Geosci.*, 2, 794-797 (2009).
- 14 Goryaeva A.M., Carrez, P. and Cordier, P. Modeling defects and plasticity in MgSiO<sub>3</sub> post-perovskite: Part 3—Screw and edge [001] dislocations. *Phys. Chem. Mineral.* 44:521–533 (2017).
- 15 Walker AR, Dobson DP., Wookey J., Nowacki A. and Forte A. The anisotropic signal of topotaxy during phase transitions in D" *Phys. Earth Planet. Inter.*, 276, 159-171 (2018).
- 16 Hunt, S.A., Walker, A.M. and Mariani, E. In-situ measurement of fabric development rate in CaIrO<sub>3</sub>. *Phys. Earth and Planet. Inter.*, 259, 91-104 (2016).
- 17 Ammann, M.W., Brodholt, J.P., Wookey, J. and Dobson, D.P. First Principles Constraints on Diffusion in Lower Mantle Minerals and a Weak D" Layer. *Nature*, 465, 462-465 (2010).
- 18 Karato, S.-i. The influence of anisotropic diffusion on the high-temperature creep of a polycrystalline aggregate. *Phys. Earth and Planet. Inter.* 183, 468–472 (2010).
- 19 Yoshino, T. and Yamazaki, D. Grain growth kinetics of CaIrO<sub>3</sub> perovskite and post-perovskite, with implications for rheology of D" layer. *Earth Planet. Sci. Lett.* 255, 485–493 (2007).
- 20 Dobson D.P., Hunt S.A., Lindsay-Scott, A. and Wood I.G. Towards better analogues for MgSiO<sub>3</sub> post-perovskite: NaCoF<sub>3</sub> and NaNiF<sub>3</sub>, two new recoverable post-perovskite phases. *Phys. Earth. Planet. Inter.*, 189, 171-175 (2011).
- 21 Lindsay-Scott, A, Dobson, D.P., Nestola, F., Alvaro, M., Casati, N., Liebske, C., Knight, K.S., Smith R. and Wood, I.G., Time-of-flight neutron powder diffraction with milligram samples: the crystal structures of NaCoF<sub>3</sub> and NaNiF<sub>3</sub> post-perovskites *J. Appl. Cryst.*, 47, 1939-194 (2014).
- 22 Lindsay-Scott, A. The thermoelastic properties of post-perovskite analogue phases. Ph.D thesis. University of London (2012).
- 23 Dobson, D.P., Thomas, R.W. and Mitchell T.M. Diffusion profiles around quartz clasts as indicators of the thermal history of pseudotachylytes. *Geochem. Geophys. Geosyst.* art. 16100914, (2018).
- 24 McCormack, R. J. *The rheological and transport properties of deep-mantle materials*. Ph.D thesis. University of London (2012).

- 25 Shirako, Y., Shi, Y.G., Aimi, A., Mori, D., Kojitani, K., Inaguma, Y. and Akaogi, M. High-pressure stability relations, crystal structures, and physical properties of perovskite and post-perovskite of  $\text{NaNiF}_3$ . *J. Solid State Chem.*, 191, 167-174 (2012).
- 26 Bravais A. *Études Crystallographic*. (Paris: Gauthier Villars) (1866).
- 27 Donnay J, Harker D. A new law of crystal morphology extending the law of Bravais. *Amer. Mineral.* 22, 446-467 (1937).
- 28 Friedel M. Etudes sur la loi de Bravais, *Bulletin de la Societe Francaise Mineralogique* 30, 326-455 (1907).
- 29 Hartman P, Bennema P. The attachment energy as a habit controlling factor: I.Theoretical considerations. *J. Cryst. Growth* 49, 145-156 (1980).
- 30 Perumal, B., Rist, M.A., Gungor, S., Brooks, J.W. and Fitzpatrick, M.E. The effect of hot deformation parameters on microstructure evolution of the  $\alpha$ -phase in Ti-6Al-4V. *Matall. Material. Trans.*, 47A, 4128-4136 (2016).
- 31 Sen, I., Kottada, R.S. and Ramamurty, U. High temperature processing maps for boron modified Ti-6Al-4V alloys. *Material. Sci. Eng. A* 527, 6157-6165 (2010).
- 32 Elliott, D. Diffusion flow laws in metamorphic rocks. *Geol. Soc. Amer.Bull.* 84, 2645-2664 (1973).
- 33 Yoon, S.Y., Akatsu, T and Yasuda, E. Anisotropy of creep deformation rate in hot-pressed  $\text{Si}_3\text{N}_4$  with preferred orientation of the elongated grains. *J. Mat. Sci*, 32, 3813-3819 (1997).
- 34 Miyazaki T, Sueyoshi K & Hiraga T Olivine crystals align during diffusion creep of Earth's upper mantle. *Nature*, 502, 321-326 (2013).
- 35 Sundberg, M and Cooper R.F. Crystallographic preferred orientation produced by diffusional creep of harzburgite: Effects of chemical interactions among phases during plastic flow. *J. Geophys. Res.* 113, B12208 (2008).
- 36 Gómez Barreiro, J., I. Lonardelli, I., Wenk H.R., Dresen G., Rybacki E., Ren Y. and Tomé C.N. Preferred orientation of anorthite deformed experimentally in Newtonian creep. *Earth Planet. Sci. Lett.* 264, 188–207 (2007).
- 37 Mancktelow, N.S. The development of slaty cleavage, Fleurieu Peninsula, South Australia. *Tectonophysics*, 58, 1-20 (1979).
- 38 McNamara, A.K., van Keken, P.E. and Karato, S.-I., Development of anisotropic structure in the Earth's lower mantle by solid-state convection. *Nature*, 416, 310-314, (2002).
- 39 Gueydan, F., Précigout, J. and Montési L.G.J. Strain weakening enables continental plate tectonics. *Tectonophysics*, 631, 189-196, (2014).
- 40 Wang Y and Wen L. Mapping the geometry and geographic distribution of a very low velocity province at the base of the Earth's mantle. *J. Geophys. Res.*, 109, B10305. (2004).

41 Hunt SA, Davies, DR, Walker, AM, McCormack, RJ, Wills, AS, Dobson, DP and Li, L. On the increase in thermal diffusivity caused by the perovskite to post-perovskite phase transition and its implications for mantle dynamics. *Earth Planet. Sci. Lett.*, 319, 96-103 (2012).

42 Ammann, MW., Walker, A.M, Stackhouse, S., Wookey, J., Forte, AM., Brodholt, JP. and Dobson, DP. Variation of thermal conductivity and heat flux at the Earth's core mantle boundary. *Earth Planet. Sci. Lett.*, 390, 175-185 (2014).

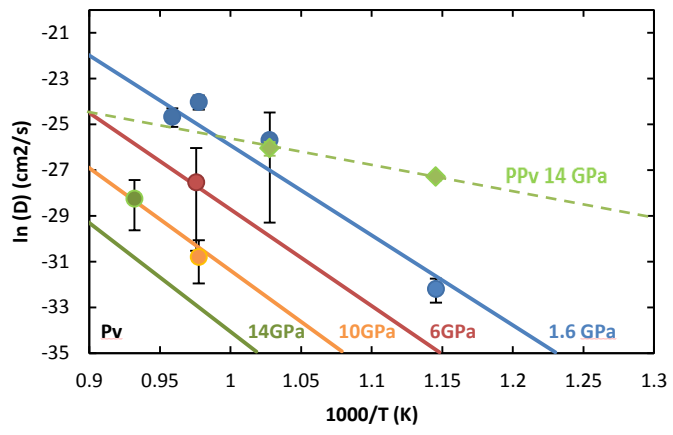
## Figure Captions

**Figure 1.** Measured Zinc chemical diffusivity in NaZnF<sub>3</sub> perovskite (circles) and post-perovskite (diamonds). The Arrhenius fit to the perovskite data at pressures of 1.6 to 10 GPa are shown as solid lines and the dashed line is the Arrhenius fit to the post-perovskite diffusion data. Data are colour-coded by pressure. Error bars are  $\pm$  two standard errors; the post-perovskite error bars are similar to the size of the symbols.

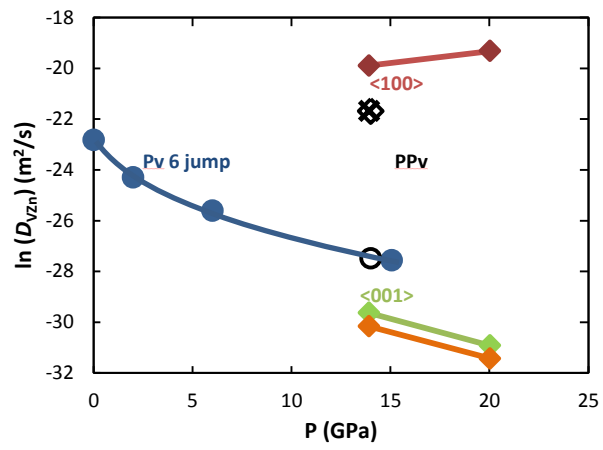
**Figure 2.** Zinc vacancy diffusivity in NaZnF<sub>3</sub> perovskite (solid diamonds) and post-perovskite (solid circles), as a function of pressure at 1073K, predicted from ab initio simulations. The diffusivity in perovskite is isotropic but post-perovskite shows  $\sim$ 4.5 orders of magnitude difference between the fastest  $\langle 100 \rangle$  and slowest  $\langle 010 \rangle$  directions. The Voigt-Reuss-Hill average of the post-perovskite axial diffusivities (cross) is 2.8 orders of magnitude higher than perovskite diffusivity at 14 GPa and 1073 K. This is in excellent agreement with the bulk-diffusivity experiments (open symbols) which are plotted after conversion to vacancy diffusivities by a constant vacancy concentration of 3.5 ppm.

**Figure 3.** A. Post-perovskite diffusion couple of a NaCoF<sub>3</sub> single crystal embedded in NaZnF<sub>3</sub>. (A) Back-scattered electron image; (B) chemical analysis profile for Cobalt in the axial and (C) radial directions. The dashed lines are best-fitting compositionally dependent diffusion profiles and the black lines are these profiles convolved by the analytical spot size. In the axial direction the effect of the convolution is smaller than the width of the line.

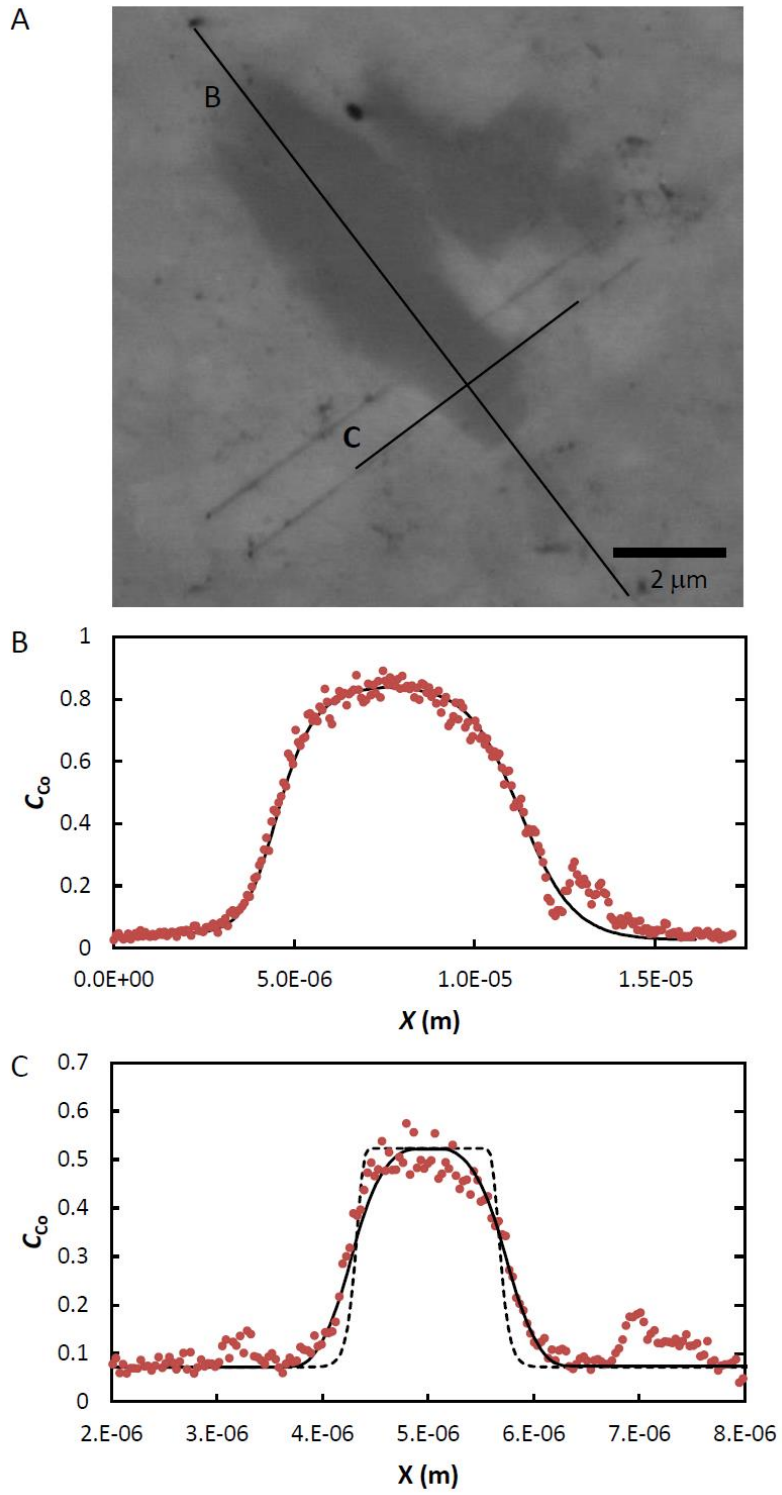
**Figure 4.** Time evolution of grain dimensions for an initially cubic crystal of MgSiO<sub>3</sub> post-perovskite of volume 1 mm<sup>3</sup> under a differential stress of 5 MPa for (A) tension parallel to a, and (B) tension parallel to c. The axial diffusivities are  $D_a=10^{-16}$  m<sup>2</sup>/s;  $D_b=10^{-22}$  m<sup>2</sup>/s;  $D_c=10^{-20}$  m<sup>2</sup>/s, consistent with ref. 17 at 120 GPa and 4000 K and a vacancy concentration of  $10^{-5}$ . The crystal axial lengths, X, Y and Z, are parallel to crystallographic axes, a, b and c and the inset shows strain rates parallel to X for situations A and B (the strain rate in Y is near zero and that in Z is equal, but opposite, to that in X). The length evolution of Y, being negligible, is omitted. Starting crystal shape and shape at maximum strain rate are sketched in (A).



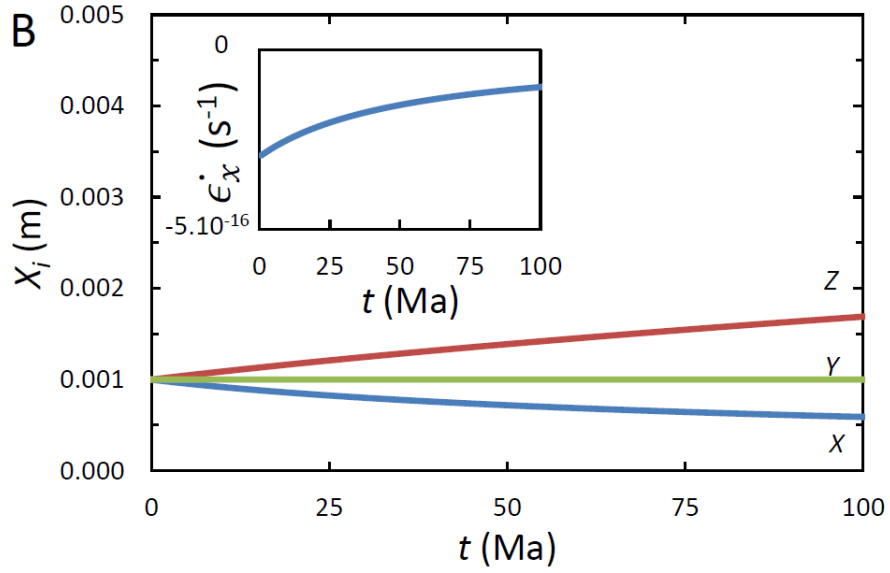
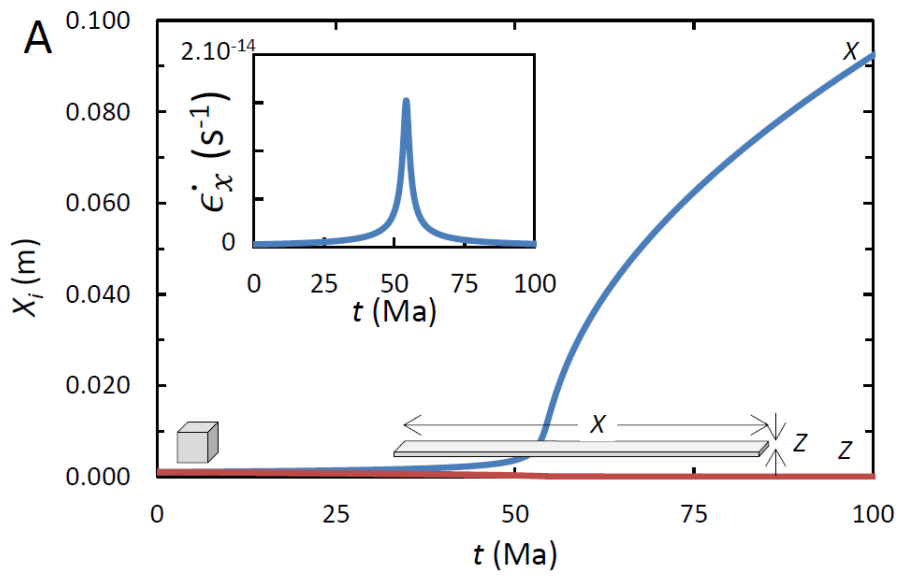
Dobson et al., figure 1



Dobson et al., figure 2



Dobson et al., figure 3



Dobson et al., figure 4



Supplementary Information for

Anisotropic diffusion creep in post-perovskite: a new model for deformation at the core-mantle boundary.

By:

David P Dobson, Alexander Lindsay-Scott, Simon A Hunt, Edward Bailey, Ian G Wood, John P Brodholt, Lidunka Vocadlo, and John Wheeler.

Corresponding author David Dobson.

Email: [d.dobson@ucl.ac.uk](mailto:d.dobson@ucl.ac.uk)

**This PDF file includes:**

Supplementary text

Figures S1 to S6

Tables S1 to S4

## **S1 Materials and Methods**

### **S1.1 Samples**

Fluoride perovskite samples were synthesised by coprecipitation from concentrated solutions of NaF and  $M(\text{NO}_3)_2$  ( $M=\text{Mn, Co, Zn, Fe}$ ). Any metal fluoride (or hydroxyfluoride) which precipitated along with the perovskite was removed by washing in a concentrated solution of  $\text{NaNO}_3$ . The resultant precipitate was then twice-washed in deionised water to produce pure fluoride perovskite as confirmed by X-ray diffraction. The fine-grained fluoride thus produced was packed in Au-foil capsules and sintered at 1 GPa and 973 K for 24 h to grow the grain-size sufficiently ( $\sim 100\mu\text{m}$ ) for grain-boundary diffusion not to be significant. Aliquots from the zinc and iron fluoride perovskites were transformed to post-perovskite at 14 GPa and 1073 K for bulk diffusivity measurements.

### **S1.2 Diffusion experiments.**

#### *Bulk diffusion experiments*

Pre-sintered polycrystalline perovskite (or post-perovskite) samples were polished to 0.3  $\mu\text{m}$  finish and placed together as a bulk-diffusion couple between  $\text{NaZnF}_3$  and either  $\text{NaMnF}_3$ ,  $\text{NaFeF}_3$ , or  $\text{NaCoF}_3$ . These couples were embedded in perovskite powders, of the same composition as the couple, within Au or Pt capsules; the metal capsules were placed in polycrystalline MgO sleeves for multi-anvil diffusion experiments. Experiments were performed by compression to the pressure of interest, followed by rapid heating to the target temperature (over  $\sim 10$  minutes with the final 100 K of heating taking less than 1 minute). The temperature was maintained, to within  $\pm 10$  K, for durations of several tens of minutes to hours after which power was cut to the furnace, resulting in quench rates of 100s of Kelvin per minute. Pressure was then slowly released at a maximum rate of 1 GPa/h and the sample recovered and sectioned parallel to the capsule axis for chemical analysis.

#### *Single-crystal diffusion experiments*

For the single-crystal post-perovskite diffusion experiments  $\text{NaCoF}_3$  post-perovskite single crystals, picked from the sample in ref<sup>20</sup>, were mixed with the  $\text{NaZnF}_3$  perovskite precipitate in a ratio of 1:100 by weight and packed in Pt foil capsules. Capsules were packed by repeatedly adding small amounts of the mixture and then tamping with a mirror-finished flat-ended steel rod to ensure that the crystals lay as flat as possible when the recovered sample was sectioned for chemical analysis. Due to the needle habit of the post-perovskite, with a-axis as the long axis and b- and c-axes approximately equal, this resulted in a final mixture with post-perovskite single crystals lying with their a-axes close to perpendicular to the packing direction and b- and c-axes randomly oriented. Experiments were performed at 14 GPa and followed the same protocol as the bulk diffusion experiments with the following exception: temperature was ramped to the target temperature at a constant rate of 100K/minute after which the temperature was quenched by cutting power to the furnace after 20 s at temperature. There is therefore likely to be a significant contribution to the measured diffusivity from diffusion during temperature ramping cycle, since the duration at temperature is very short. Recovered samples were sectioned perpendicular to the axis of the capsule to reveal  $\text{NaCoF}_3$  post-perovskite single crystals with their a-axes lying in the plane of the section.

#### *Chemical analysis*

Recovered and sectioned samples were polished under water, finishing with 0.3  $\mu\text{m}$  alumina, and then coated with 7 nm of carbon for chemical analysis. Samples were analysed using a LEO Gemini 1530 FEG SEM at 15 kV accelerating voltage and 4 nA beam current in high resolution mode. Chemical profiles, perpendicular to the diffusion interface were collected and, additionally for the single-crystal samples, 2-dimensional compositional maps were collected in energy dispersive mode using Link ISIS software. Due to strong interferences between the escape peaks of the divalent metal species and the K-lines of fluorine and sodium it was not possible to perform quantitative ZAF corrections. Instead zinc compositional profiles from interdiffusion experiments were analysed in the form  $C_A = \{A\} / (\{A\} + \{B\})$ , where  $\{A\}$  and  $\{B\}$  are the raw X-ray counts of the two divalent metals in the interdiffusion couple (Zn, Mn, Co, Fe). Errors due to differences in ZAF parameters between the divalent species are negligible due to their similar atomic numbers and the fact that they are significantly heavier than either fluorine or sodium.

### **S1.3 Diffusion profile fitting**

Diffusion profiles were fitted using a Boltzmann-Matano formulation (eg ref. S1) since the interdiffusion coefficient was found to be compositionally dependent. In this case, the concentration-dependent interdiffusion coefficient of a species,  $\bar{D}(c)$ , at position  $z$  from the Matano interface is given by:

$$\bar{D}(c) = -\frac{1}{2t} \frac{\int_c^{c_0} z dc}{(dc/dz)_c} \quad (\text{M1}),$$

where the concentrations at plus and minus infinity are  $C_0$  and  $C_1$  respectively. The Matano interface, where the flux of atoms in the positive and negative directions is equal, is given by:

$$0 = \int_{c_0}^{c_1} (z - z_0) dc \quad (\text{M2}).$$

An appropriate functional form is fitted to the experimental data and then equations M1 and M2 are applied to the fit. We used a sigmoidal function which is appropriate for diffusion of vacancies of heterovalent species in ionic crystals<sup>S2</sup> :

$$x = A_0 \left( 1 - \frac{1}{(1 + e^{A_1 x + A_2})^{A_3}} \right) + A_4 \quad (\text{M3}).$$

An example of the fit and resultant concentration-dependent diffusivity is presented in figure S1. The sigmoidal functions fit the experimental data extremely well at most compositions. However, close to the extrema in composition the integral (equation M1) deviates strongly and the end-member diffusivities are derived by extrapolation of a linear fit to mid-range values ( $0.1 < C_{\text{Zn}} < 0.9$ ) of  $\bar{D}(c)$ . For comparison with the simulations, performed for pure  $\text{NaZnF}_3$ , exponential fits to the integral were extrapolated to the end-member compositions (Fig. S1b). We have chosen here to concentrate on the diffusivities of the Zn end-member for several reasons: First, its solely divalent state gives it the simplest point-defect chemistry for comparison with the *ab initio* simulations; Second,  $\text{Zn}^{2+}$  is non-magnetic which significantly simplifies the simulations; Third, the post-perovskite form of  $\text{NaZnF}_3$  forms at slightly lower pressure (10-12 GPa) than the other compositions and is fully recoverable, making it ideal for the matrix of the single-crystal simulations.

### *Fitting single-crystal data.*

Post-perovskites grow as long needles with their  $a$ -axes as the needle direction<sup>20-22</sup>; in the case of the crystals used here the long dimension was up to  $3\mu\text{m}$  and the short dimension was  $\sim 0.5\mu\text{m}$ . Line profiles (in the axial and radial directions) were collected from the diffusion-annealed sample and these were fitted independently. In this case the diffusion couple is between a  $\text{NaCoF}_3$  single crystal and a  $\text{NaZnF}_3$  polycrystalline matrix hence the local diffusivity at each point includes a compositional dependence and a crystallographic dependence. Since we are interested in the end-member single-crystal and bulk diffusivities a Boltzmann-Matano analysis was performed and the reported single-crystal and matrix diffusivities are the fitted values at the end-member compositions at the centre of the crystal and in the matrix respectively. The profiles thus calculated fitted the observed profiles to within the observational error (see Figure 3 of main text). The extremely short diffusion profiles necessary in the single-crystal study caused the SEM analytical spot size to become significant for the profiles in the slow diffusion direction. A Gaussian beam-convolution was therefore added to the calculated diffusion profiles for comparison with the observations. This convolution was determined by cold-pressing a couple comprising  $\text{NaMnF}_3$  and  $\text{NaCoF}_3$  perovskite with each surface of the couple having been polished to mirror finish using  $0.1\mu\text{m}$  diamond abrasive. The interface of the recovered couple remained sharp and the apparent profile was well fitted with a Gaussian convolution with standard deviation of  $0.35\mu\text{m}$  (Figure S2). The convolution was applied to the calculated diffusion profiles as a weighted boxcar average with the weightings following a Gaussian profile ( $\sigma=0.35\mu\text{m}$ ) about the centroid of the boxcar. Fitted single-crystal and matrix diffusivities are given in Table S2.

To check the assumptions inherent in these fits of; (1) independent diffusion in each direction and, (2) composition dependence also accounting for matrix dependence, we collected a compositional map from one crystal. This was compared with a finite difference model (based on the model of reference<sup>S3</sup>) which incorporated the axial-, and radial-single-crystal, and bulk diffusion coefficients derived from the Boltzmann-Matano analyses of the line profiles (Figure S3).

### **S1.4 *Ab initio* simulations**

Zinc-vacancy diffusion coefficients for  $\text{NaZnF}_3$  perovskite and post-perovskite were calculated from first principles using Vineyard Theory implemented in the Vienna Ab Initio Simulation Package as described previously<sup>11, S4-S5</sup>.

The *ab initio* calculations used the projector augmented wave implementation<sup>S6-S7</sup> of the density functional theory<sup>S8-S9</sup> with the generalised gradient approximation (GGA) PBE pseudopotentials<sup>S10</sup>. An electronic minimization convergence criterion of  $10^{-6}$  eV was used for the internal energy. A  $k$ -point density of  $6 \times 6 \times 6$ <sup>S11</sup> and an energy cutoff of 1000 eV were found to be sufficient to produce changes of less than  $0.001$  eV  $\text{atom}^{-1}$  in the calculated internal energy.

Migration enthalpies were calculated for the direct jump and the 6-jump cycle found to be fastest for Zn in perovskite in all directions and in the  $\langle 010 \rangle$  direction in post-perovskite. The attempt frequencies of  $\text{MgSiO}_3$  perovskite and post-perovskite close to their equilibrium boundaries were used for the present calculations on  $\text{NaZnF}_3$ . While this might cause some error in absolute diffusivity values, it is unlikely to significantly affect the relative diffusivities between phases and

directions as the difference in attempt frequency is a factor of two between the highest and lowest frequencies. The largest error in predicting chemical diffusivity from the simulations arises from uncertainty in the vacancy concentration. In ionic compounds of multivalent transition metals, such as those under investigation here the dominant vacancies are likely to be extrinsic due to either impurities or redox-induced non-stoichiometry. We therefore treat the vacancy concentration as a single adjustable parameter. A not-unreasonable vacancy concentration of 3.5 ppm is required to bring the ab initio simulations into close agreement with the bulk diffusion experiments. (See Ammann et al 2010<sup>17</sup> supplementary information for additional information on the method)

The simulated activation enthalpies found here and other parameters used in the Vineyard equation are given in Table S3.

### **S1.5 Errors**

We consider that there are two main sources of error in the single crystal study: geometric errors and resolution limitations. Here we argue that the sources of error will tend to reduce the apparent anisotropy observed in the present experiments and that the quoted experimental anisotropy of three orders of magnitude is likely to underestimate the true value, possibly significantly so.

#### *Geometric errors*

In the single-crystal diffusion experiments there are several errors which can arise due to the geometry and orientation of the crystal with respect to the analytical plane. Consider an acicular crystal embedded in an isotropic matrix intersected by an arbitrary plane as shown in figure S4. In the case of a crystal whose long axis intersects the plane on which analyses are performed at an angle,  $\theta$ , (fig. S4 A) there is an artificial lengthening of the profile in the axial direction by either  $D' = D_r / \sin\theta$ , or  $D'' = D_a / \cos\theta$ , where  $D'$  and  $D''$  are the apparent profiles observed for true profiles,  $D_r$  and  $D_a$ , in faces parallel and perpendicular respectively to the long axis. Measured radial diffusion gradients are primarily influenced by how close the long axis of the crystal is to the surface (crystals B and C in figure S4). For a crystal of radius,  $r$ , surrounded by a diffusion profile of length  $D_r$ , the apparent profile length is  $D^* = (r + D_r) \sin\phi - r \sin\iota$ , where the angles subtended by the chords made by the intersection of the analytical plane with the diffusion profile are  $\phi$  and  $\iota$  respectively. It can be seen, therefore, that in all cases apparent diffusion profiles in the radial direction can never be shorter than true diffusion profiles and that the matrix diffusivity will be just as affected by these errors as the single-crystal values.

We therefore have several checks on the accuracy of the observed single-crystal diffusivities:

- 1 The packing and sectioning procedure was developed to try to minimise the angular mismatch between the long axis and the analysis section;
- 2 Analyses which showed a significant difference in axial diffusion between one end and the other were rare and those which did show significant difference were discarded;
- 3 The variability of measured diffusivity in each direction was low, being 10% for the axial direction and 50% for the radial direction. This might mean that the radial direction was more affected by the geometric errors discussed above, but equally since the crystal orientation was not determined this might represent a true variability between diffusion in the crystallographic  $b$  and  $c$  directions.

4 The matrix diffusivity agrees to within 1 standard error for measurements from either radial or axial profiles whereas the crystal values differ by 3 orders of magnitude on average. The sources of error discussed above should affect the apparent matrix diffusivity equally as much as the crystal diffusivity suggesting that the observed differences between axial and radial diffusivities are genuine.

5 Possibly the most robust measurements are those with the shortest profiles, which give diffusion coefficients of  $5.17 \times 10^{-14} \text{ cm}^2/\text{s}$  and  $4.59 \times 10^{-18} \text{ cm}^2/\text{s}$  respectively in the axial and radial directions, showing 4 orders of magnitude of anisotropy, in close agreement with the simulations.

#### *Resolution limitation*

The observed radial diffusion profiles are very short, close to the resolution of the SEM spot. Use of larger crystals or a smaller analytical spot would solve this, but this was unfortunately not possible. Attempts at flux-growing large single crystals of post-perovskite produced radiating arrays of extremely fine needles with aspect ratios in excess of 10 which were very difficult to separate without damaging them. Furthermore, the fluoride post-perovskites are quite weakly metastable; they back-transform to perovskite at  $\sim 473\text{K}$  and readily decompose during transmission electron microscopy. This weak metastability also impeded EBSD determination of crystal orientation in the single-crystal diffusion couple. We are therefore confined to measuring short diffusion profiles in the SEM and using a beam profile convolution to model the finite analytical volume as discussed above. This convolution improves the accuracy of measurements for short profiles, but there is still a lower limit to the diffusion coefficient measurable from the diffusion profile lengths: here we consider this to be  $2 \times 10^{-18} \text{ cm}^2/\text{s}$  in the single-crystal experiment when the beam convolution will contribute 80% of the observed signal. The shortest radial diffusion profile did come close to this resolution limit suggesting that perhaps the slowest diffusion direction might be too slow for accurate measurement in this study.

## S2 The Crystal chemistry of extreme anisotropic diffusion creep in post-perovskite.

The post-perovskite structure can be viewed as sheets of interconnected octahedral  $\text{SiO}_6$  units separated by layers of magnesium in 8-fold coordination. The silica octahedra are edge-sharing in the a-crystallographic direction and corner sharing in the c-direction defining the unit-cell parameters in those directions as 2.46 Å and 6.09 Å for  $\text{MgSiO}_3$  post-perovskite<sup>1</sup>. A triangular prismatic interstitial volume exists between the Mg-O and Si-O coordination polyhedra. This interstitial volume is repeated by stacking on its basal pinnacoid to create an interconnected channel running parallel to the a-axis. The b-axial direction is longer (8.042 Å), encompassing both the silica and magnesia layers. The anisotropy of chemical diffusion in this structure can be explained by consideration of the ease of hopping in the various axial directions. For diffusion along a (the fastest diffusion direction) the jump distances are smallest, Si moves between edge-sharing octahedra and Mg can utilise the interstitial channel during the hop from one Mg site to the next. Diffusion along c (the intermediate direction) has an intermediate hop distance and requires hopping of Si between corner sharing octahedra and Mg across face-sharing Mg-O polyhedra. Diffusion in the slowest, b, direction involves the largest distance of hop and requires both Mg and Si to traverse the sheets containing the other species. The hopping distance and the degree of connectivity of coordination polyhedra have been invoked to explain the observed diffusion anisotropy in feldspar and olivine respectively<sup>5,12</sup>. While both of these considerations apply to post-perovskite the anisotropy in  $\text{MgSiO}_3$  is extremely large. This is due to the effect of pressure. Diffusion is a thermally activated process with the activation energy comprising an enthalpy and a volume component:  $E = \Delta H + P\Delta V$ . The values of activation enthalpy and activation volume are positively correlated, both arising from the local atomic strains required during the hopping of an atom or ion from one site to another. This results in diffusion processes with a large activation enthalpy being more sensitive to pressure and hence an increase in anisotropy with increasing pressure. This is seen in figure 2 where an increase of 6 GPa in pressure increases the anisotropy of diffusion in  $\text{NaZnF}_3$  post-perovskite by a factor of 3. In the case of magnesium silicate post-perovskite the activation enthalpies for vacancy diffusion in the a, b and c directions are 3.43, 13.76 and 7.95 eV and the activation volumes are 1.29, 3.58 and 2.15  $\text{cm}^3/\text{mole}$  respectively at 121.5 GPa<sup>17</sup>.

## S3 Diffusion creep.

Lattice-diffusion creep operates by diffusion of vacancies through a crystal, from sources to sinks at crystal surfaces, combined with grain rotations and grain-boundary sliding. For the case of isotropic diffusion and equant grain shapes, the classical Nabarro-Herring equation takes the form:

$$\dot{\epsilon} = \frac{AD\sigma\Omega}{g^2kT} \quad \text{S1,}$$

where  $\dot{\epsilon}$  is the strain rate,  $A$  is a geometric constant,  $D$  is the self-diffusion coefficient,  $\sigma$  is the applied stress,  $\Omega$  is the atomic volume,  $g$  is the grain size,  $k$  is the Boltzmann constant and  $T$  is the absolute temperature. We consider two possible cases of anisotropy in diffusion creep in post-perovskite: anisotropic crystal shape and anisotropic chemical diffusivity. First we consider the effect of shape anisotropy in a material with isotropic chemical diffusivity and then extend this to include anisotropic diffusivity.

### S3.1 Anisotropic creep due to grain shape

For the case of principal tensile stresses,  $\sigma_i$ , acting along the axes,  $x, y, z$  of a crystal taking the form of a rectangular parallelepiped of dimensions  $\pm X/2, \pm Y/2, \pm Z/2$ , as cartooned in figure S5, the analytical form for the steady-state strain rates in the axial directions,  $\dot{\epsilon}_i$ , is<sup>S13</sup>:

$$\dot{\epsilon}_x = \frac{AD\Omega}{kT} [\sigma_x(Y^2 + Z^2) - \sigma_y Z^2 - \sigma_z Y^2] / [X^2 Y^2 + Y^2 Z^2 + X^2 Z^2];$$

$$\dot{\epsilon}_y = \frac{AD\Omega}{kT} [\sigma_y(Z^2 + X^2) - \sigma_z X^2 - \sigma_x Z^2] / [X^2 Y^2 + Y^2 Z^2 + X^2 Z^2];$$

$$\dot{\epsilon}_z = \frac{AD\Omega}{kT} [\sigma_z(X^2 + Y^2) - \sigma_x Y^2 - \sigma_y Z^2] / [X^2 Y^2 + Y^2 Z^2 + X^2 Z^2],$$

or in matrix notation:

$$\begin{bmatrix} \dot{\epsilon}_x \\ \dot{\epsilon}_y \\ \dot{\epsilon}_z \end{bmatrix} = \frac{AD\Omega}{kT} \begin{bmatrix} (Y^2 + Z^2)/\beta & -Z^2/\beta & -Y^2/\beta \\ -Z^2/\beta & (Z^2 + X^2)/\beta & -X^2/\beta \\ -Y^2/\beta & -X^2/\beta & (X^2 + Y^2)/\beta \end{bmatrix} \begin{bmatrix} \sigma_x \\ \sigma_y \\ \sigma_z \end{bmatrix} \quad \text{S2,}$$

where  $\beta = [X^2 Y^2 + Y^2 Z^2 + X^2 Z^2]$ ,  $D$  is a scalar self-diffusion coefficient and  $A=12$ . Suppose that  $X \gg Y$  and  $Z$ , so grains are needle-shaped, then approximately

$$\begin{bmatrix} \dot{\epsilon}_x \\ \dot{\epsilon}_y \\ \dot{\epsilon}_z \end{bmatrix} \cong \frac{AD\Omega}{kT} \begin{bmatrix} 1/X^2 & -Z^2/(Y^2 + Z^2)X^2 & -Y^2/(Y^2 + Z^2)X^2 \\ -Z^2/(Y^2 + Z^2)X^2 & 1/(Y^2 + Z^2) & -1/(Y^2 + Z^2) \\ -Y^2/(Y^2 + Z^2)X^2 & -1/(Y^2 + Z^2) & 1/(Y^2 + Z^2) \end{bmatrix} \begin{bmatrix} \sigma_x \\ \sigma_y \\ \sigma_z \end{bmatrix} \quad \text{S3.}$$

This demonstrates there is strain rate (mechanical) anisotropy; the strain rate depends on  $1/L^2$  where  $L$  is the length of the crystal in the direction of strain. For needles, with an aspect ratio of 100:1:1, changing the stress parallel to the long dimension ( $\sigma_x$ ) gives a  $10^4$  times smaller effect on strain rate than changing the stress in the transverse directions  $\sigma_y$  or  $\sigma_z$  (for a material with isotropic chemical diffusivity) because  $1/X^2$  is small. If the aspect ratio is 10:1:1 this strain rate anisotropy would be 1:100:100 and for an aspect ratio of unity equation S3 is identical to S1.

### S3.2 Anisotropic creep due to anisotropic diffusivity

Since equations S2 and S3 are steady-state solutions they can be generalised to cases of anisotropic diffusivity<sup>S13</sup> where the principal axes of diffusion are parallel to the edges of the rectangular crystal,  $x||a; y||b; z||c$ . In this case, we stipulate that  $\bar{D}$  is the geometric mean,  $\bar{D}^3 = D_{11} \times D_{22} \times D_{33}$ , of the anisotropic diffusion tensor:

$$\mathbf{D} = \begin{bmatrix} D_{11} & 0 & 0 \\ 0 & D_{22} & 0 \\ 0 & 0 & D_{33} \end{bmatrix} \quad \text{S4.}$$

Here we use the indices  $D_{ii}$  to denote a general anisotropic diffusion tensor. We distinguish this from the specific diffusion tensor of  $\text{MgSiO}_3$  post-perovskite by replacing the indices with crystallographic directions,  $D_{11} = D_a; D_{22} = D_b; D_{33} = D_c$ , for the post-perovskite system.

A Lagrange transform is applied to the spatial coordinate system<sup>S14</sup>:

$$x = x' \sqrt{D_{11}/\bar{D}}; \quad y = y' \sqrt{D_{22}/\bar{D}}; \quad z = z' \sqrt{D_{33}/\bar{D}} \quad \text{S5.}$$

This transform can be viewed as a volume-conserving homogeneous strain and hence source and sink strengths and compositional isograds are conserved. It can be further shown<sup>S14</sup> that fluxes are also conserved under this transform. In the transformed coordinate system the diffusivities are isotropic and the solutions of ref.<sup>S13</sup> apply; S2 becomes:

$$\begin{bmatrix} \dot{\epsilon}_x \\ \dot{\epsilon}_y \\ \dot{\epsilon}_z \end{bmatrix} = \frac{A\Omega}{kT} \begin{bmatrix} (Y'^2 + Z'^2)/\beta & -Z'^2/\beta & -Y'^2/\beta \\ -Z'^2/\beta & (Z'^2 + X'^2)/\beta & -X'^2/\beta \\ -Y'^2/\beta & -X'^2/\beta & (X'^2 + Y'^2)/\beta \end{bmatrix} \begin{bmatrix} \sigma_x \\ \sigma_y \\ \sigma_z \end{bmatrix} \quad \text{S6}$$

and similarly for S3. Applying the substitution S5 we obtain the equation for anisotropic diffusivity in the real space coordinate system:

$$\begin{bmatrix} \dot{\epsilon}_x \\ \dot{\epsilon}_y \\ \dot{\epsilon}_z \end{bmatrix} = \frac{A\Omega}{kT} \begin{bmatrix} \left(\frac{Y^2}{D_{22}} + \frac{Z^2}{D_{33}}\right)/\gamma & -\frac{Z^2}{D_{33}}/\gamma & -\frac{Y^2}{D_{22}}/\gamma \\ -\frac{Z^2}{D_{33}}/\gamma & \left(\frac{X^2}{D_{11}} + \frac{Z^2}{D_{33}}\right)/\gamma & -\frac{X^2}{D_{11}}/\gamma \\ -\frac{Y^2}{D_{22}}/\gamma & -\frac{X^2}{D_{11}}/\gamma & \left(\frac{Y^2}{D_{22}} + \frac{X^2}{D_{11}}\right)/\gamma \end{bmatrix} \begin{bmatrix} \sigma_x \\ \sigma_y \\ \sigma_z \end{bmatrix} \quad \text{S7,}$$

and  $\gamma = \left[\frac{X^2}{D_{11} D_{22}} + \frac{Y^2}{D_{22} D_{33}} + \frac{X^2}{D_{11} D_{33}}\right]$ . In the case of isotropic grain shape  $X = Y = Z$ , this further simplifies to:

$$\begin{bmatrix} \dot{\epsilon}_x \\ \dot{\epsilon}_y \\ \dot{\epsilon}_z \end{bmatrix} = \frac{A\Omega}{kTX^2} \begin{bmatrix} (D_{11}D_{33} + D_{11}D_{22})/\vartheta & -D_{11}D_{22}/\vartheta & -D_{11}D_{33}/\vartheta \\ -D_{11}D_{22}/\vartheta & (D_{11}D_{22} + D_{22}D_{33})/\vartheta & -D_{22}D_{33}/\vartheta \\ -D_{11}D_{33}/\vartheta & -D_{22}D_{33}/\vartheta & (D_{11}D_{33} + D_{22}D_{33})/\vartheta \end{bmatrix} \begin{bmatrix} \sigma_x \\ \sigma_y \\ \sigma_z \end{bmatrix} \quad \text{S8,}$$

where  $\vartheta = (D_{11} + D_{22} + D_{33})$ .

Table S4 lists the anisotropy of strain rate from equations S8 for cubic grain shape and several cases of diffusion anisotropy: prolate anisotropy ( $D_{11} > D_{22} = D_{33}$ ), oblate anisotropy ( $D_{11} < D_{22} = D_{33}$ ) and general orthorhombic anisotropy ( $D_{11} > D_{22} > D_{33}$ ) deforming under pure shear.

To understand the anisotropy in more detail, first consider a plane strain situation in which (for example)  $\dot{\epsilon}_y$  is set to zero. Then equation S8 can be used to determine  $\sigma_y$  in terms of  $\sigma_x$  and  $\sigma_z$  and the other strain rates can be calculated in terms of the differential stress:

$$\dot{\epsilon}_x = \frac{A\Omega}{kT\left(\frac{X^2}{D_{11}} + \frac{Z^2}{D_{33}}\right)} (\sigma_x - \sigma_z) \quad \text{S9}$$

This shows that when deforming solely in the XZ plane in crystals with small shape anisotropy, it is the *slower* of the two diffusion coefficients which is rate-determining, because the intracrystalline diffusion pathways are curved and diffusion is hampered when the path turns into the slower direction. In 3D strain the pathways are generally curved in 3D and all three diffusion coefficients have an effect. Consider a diffusion tensor with  $D_{11} \gg D_{22}, D_{33}$ , then S8 for a cubic grain becomes

$$\begin{bmatrix} \dot{\epsilon}_x \\ \dot{\epsilon}_y \\ \dot{\epsilon}_z \end{bmatrix} \cong \frac{A\Omega}{kTX^2} \begin{bmatrix} (D_{33} + D_{22}) & -D_{22} & -D_{33} \\ -D_{22} & D_{22} & 0 \\ -D_{33} & 0 & D_{33} \end{bmatrix} \begin{bmatrix} \sigma_x \\ \sigma_y \\ \sigma_z \end{bmatrix} \quad \text{S10,}$$

This shows that the two slower diffusion coefficients contribute to the anisotropy. If we further propose that  $D_{33} \gg D_{22}$ , as for post-perovskite, S10 becomes

$$\begin{bmatrix} \dot{\epsilon}_x \\ \dot{\epsilon}_y \\ \dot{\epsilon}_z \end{bmatrix} \cong \frac{A\Omega}{kTX^2} \begin{bmatrix} D_{33} & 0 & -D_{33} \\ 0 & 0 & 0 \\ -D_{33} & 0 & D_{33} \end{bmatrix} \begin{bmatrix} \sigma_x \\ \sigma_y \\ \sigma_z \end{bmatrix} \quad \text{S11,}$$

which shows that, for a cubic grain shape, the faster creep rates are controlled by the *second* fastest diffusion direction, with creep rate being very slow parallel to the slow diffusion direction (unless huge stresses are applied in that direction).

In the case of  $\text{MgSiO}_3$  post-perovskite ( $D_a \sim 10^{-16} \text{m}^2/\text{s}$ ;  $D_b \sim 10^{-22} \text{m}^2/\text{s}$  and  $D_c \sim 10^{-20} \text{m}^2/\text{s}$  at 120 GPa and 4000 K<sup>17</sup>, with a vacancy population of  $10^{-5}$ ) with equant crystals, the anisotropy of the strain response (eqn S10) would therefore be  $\dot{\epsilon}_x \approx \dot{\epsilon}_z \approx 100\dot{\epsilon}_y$ .

#### S4 Effect of combined shape and diffusion anisotropy on creep

Consider the evolution of an initially cubic grain of post-perovskite in a plane strain scenario, so that grain area  $G = XZ$  is conserved. For isotropic diffusion, elongate grains are stronger than equant grains of equivalent area as shown by eqn (S9), see also eqn 5 of reference 28. For anisotropic diffusion, the strain rate given by eqn (S9) has a *maximum* at  $X/Z = \sqrt{(D_{11}/D_{22})}$ , or  $X = (D_{11}/D_{22})^{1/4} X_0 \approx 10 X_0$  before decreasing as hardening is established. This is because the rate limiting diffusion direction relates to the direction with the second largest value of  $D_i/X_i^2$  where the subscript,  $i$ , denotes the  $i$ th direction. This is shown graphically in Figure 4 where equation (7) is propagated in time for an initially cubic grain of  $1 \text{ mm}^3$  and chemical diffusivities of  $D_a = 10^{-16} \text{m}^2/\text{s}$ ;  $D_b = 10^{-22} \text{m}^2/\text{s}$  and  $D_c = 10^{-20} \text{m}^2/\text{s}$ , appropriate for  $\text{MgSiO}_3$  post-perovskite at the core-mantle boundary, and a differential stress of 5 MPa. As expected there is virtually no strain in the slow (crystallographic  $b$ ) diffusion direction, but the behaviour in the fast ( $a$ ) and intermediate ( $c$ ) directions varies substantially depending on whether the fast direction is in tension or compression. For the case of compression along  $a$  (Figure 4b), the strain rate is limited by  $D_c/Z^2$  and, as  $Z$  increases with strain, the crystal exhibits strain hardening behaviour. For the case of tension along  $a$  (Figure 4a) the strain rate is also initially controlled by  $\dot{\epsilon} \sim D_c/Z^2$ , but now the crystal is stretching in  $X$  and shrinking in  $Z$ , resulting in an acceleration in the rate limiting process, diffusion along  $c$ . The crystal therefore exhibits a strain weakening rheology until  $X \approx 100 Z$ , after which the limiting process switches to diffusion along  $x$  with  $\dot{\epsilon} \sim D_a/X^2$ . Further strain then results in increasing viscosity as the  $X$ -dimension continues to grow. However, by the time the rheology switches from one of strain weakening to strain hardening the initially cubic crystal has evolved to dimensions of  $X=11 \text{ mm}$ ,  $Y=1 \text{ mm}$ ,  $Z=0.09 \text{ mm}$  which, as we argue in the main text, is likely to be susceptible to breaking during shear-induced rotations and hence reduction of the long dimension of the crystal.

#### S5 Generation of shape- and crystallographic-preferred orientation due to anisotropic diffusion creep

So far we have shown that an anisotropic diffusion tensor will result in anisotropic diffusion creep in single crystals. We now discuss some implications of this for generation of crystallographic preferred orientations and for rheological laws in polycrystals. Consider the directions of strain generated in a crystal of cubic shape with crystallographic axes parallel to the cube vertices, as in the

foregoing discussion, where the stresses acting on the crystallographic axes are:  $\sigma_1 = \sigma_m$ ;  $\sigma_2 = \sigma_m + \delta\sigma$ ;  $\sigma_3 = \sigma_m - \delta\sigma$ . In the case of isotropic diffusivity this would result in a pure shear in the (011) plane of the crystal as illustrated in Figure S6a. For general orthorhombic anisotropy with  $D_{11} \gg D_{22} \gg D_{33}$  (Table S4) these stresses result in out-of-plane crystal strains with mass flux from (010) faces to (100) faces with resultant strains as illustrated in figure S6b. The key point here is that crystals will acquire shapes in which the slow diffusion direction is parallel to the axis of intermediate length. Elongate shapes are likely to rotate, as shown in precise grain-scale models for grain boundary diffusion (Coble) creep<sup>S15-S16</sup>, but there is no comparable model for Nabarro-Herring creep. However, a wide variety of models for objects (e.g. triaxial ellipsoids) embedded in a medium of different rheology<sup>S17-S19</sup> show that grains will rotate so that the long axis is parallel to the shear direction and the intermediate axis is perpendicular to the shear profile plane. We propose this will occur here, and in so doing, the plane containing the faster diffusion directions aligns with the profile plane, where differential stress is at a maximum. It follows that post-perovskite should display a strain-weakening rheology since the developing CPO results in increasing numbers of grains oriented in the fastest straining orientation. There is a second process we propose that leads to strain softening. Imagine stressing 2 equant grains, one (P) with  $D_{11}$  perpendicular to  $\sigma_1$  and the other (Q) with  $D_{11}$  parallel to  $\sigma_1$ . According to section S4, grain P will strain soften and grain Q will strain harden. This means that grains in similar orientations to P will elongate more quickly and will likely rotate more quickly than those similar to Q, suggesting that  $D_{11}$  will evolve preferentially to be parallel to the shear direction. Since, for elongations less than 100, such grains strain soften, this is an additional cause of weakening in the overall polycrystal. This combination of passive rotation and active intracrystalline deformation is no different to standard explanations of fabric development in crustal rocks, for which there is abundant evidence, e.g. Chapter 14 of reference S20, - though the prediction of this type of consequent weakening is novel. The prediction of CPOs which anisotropic diffusion creep might lead to is beyond the scope of the present paper but we suggest that embedded particle in continuum modelling akin to the VPSC method might be a fruitful first step.

### **S6 Diffusion creep versus dislocation creep in D''**

On the basis of the calculated diffusivity in magnesium silicate post-perovskite Ammann et al.<sup>17</sup> concluded that post-perovskite would be stronger than perovskite in D'' when deforming by diffusion creep and so concentrated on the effects of the calculated diffusivity on dislocation creep in post-perovskite. This was based on volumetric averaging of the diffusion tensor over  $10^6$  randomly oriented cubic crystals and resulted in a viscosity about 1 order of magnitude higher than that derived from equation S11 for diffusivity values of magnesium silicate post-perovskite and 2 orders of magnitude higher than the viscosity of perovskite. Given this result, coupled with the observation of strong anisotropy in D'', they chose to concentrate on the effects of post-perovskite diffusivity on dislocation creep, concluding that post-perovskite is weaker than perovskite deforming in dislocation creep. A similar conclusion has recently been drawn on the basis of simulations of climb-assisted dislocation glide and pure climb plasticity in perovskite and post-perovskite<sup>14,S22-S23</sup>, concluding that post-perovskite is weaker than perovskite and that dislocation mechanisms dominate for grain sizes above about  $10^{-1}$  mm at mantle strain rates. Those studies also used diffusivity values from<sup>17</sup>. This critical grain size is very close to the grain sizes predicted from laboratory grain growth studies of bridgmanite<sup>S24</sup> and so there is a realistic possibility that pure climb might control the rheology of perovskite-dominated regions. For anisotropic diffusion creep in post-perovskite these arguments are modified by the coupling between diffusivity and grain size

(equation S7) which implies that for needle-like post-perovskite crystal shapes with aspect ratios of 100:1 dislocation creep would dominate in  $D''$  only for needle lengths of 10 mm or more. This is likely to be unrealistically large since (1) shear processes break needles as discussed above, (2) the grain size of post-perovskite after transformation from perovskite will be smaller than the original perovskite grain size, possibly substantially so, based on experiments investigating the transformation mechanism<sup>12</sup> and (3) the free-slip condition at the core-mantle boundary means that stresses in the lowermost mantle will be very small. It is possible that immediately surrounding subducting slabs the stresses might be sufficiently high to support dislocation creep in limited areas in  $D''$ , as suggested by<sup>38</sup> but the majority of  $D''$  is more likely to be deforming by diffusion creep.

### S7 Note on nomenclature

Natural mineral samples of perovskite-structured  $(\text{Mg,Fe})\text{SiO}_3$  are called bridgmanite. Here we use the term perovskite for synthetic samples since we are primarily interested in the differences in properties between materials in the perovskite and post-perovskite structures. For clarity we also use the term 'perovskite' or  $\text{MgSiO}_3$ -perovskite in our discussion for natural bridgmanite which is postulated to be the main phase in the lower mantle and, possibly, in hot regions of  $D''$ .

### Supplementary references

- S1. Crank, J. The mathematics of Diffusion. Second Edition. Oxford University Press, (1975).
- S2. Mackwell, S., Bystricky, M. and Sproni, C. Fe-Mg Interdiffusion in  $(\text{Mg,FeO})$ . *Phys. Chem. Mineral.*, 32, 418-425 (2005).
- S3. Watson, E.B., Wanser, K.H. and Farley K.A. Anisotropic diffusion in a finite cylinder, with geochemical applications. *Geochim. Cosmochim. Acta*, 74, 614–633 (2010).
- S4. Kresse G., Furthmüller J. Efficiency of ab-initio total energy calculations for metals and semiconductors using a plane-wave basis set. *Comput. Mater. Sci.* 6:15-50 (1996).
- S5. Kresse, G., Marsman, M. and Furthmüller, J. VASP Guide. Faculty of Physics, Universität Wien, Austria <http://cms.mpi.univie.ac.at/vasp/vasp/vasp.html> (2016).
- S6. Blöchl P.E. Projector augmented-wave method. *Phys. Rev. B* 50:17953–17979 (1994).
- S7. Kresse G., Joubert J. From ultrasoft pseudopotentials to the projector augmented wave method. *Phys. Rev. B* 59:1758–1775 (1999).
- S8. Hohenberg P., Kohn W. Inhomogeneous electron gas. *Phys. Rev.* 136:864-871 (1964).
- S9. Kohn W., Sham L.J. Self-consistent equations including exchange and correlation effects. *Phys. Rev.* 140:A1133-A1138 (1965).
- S10. Perdew J.P., Burke K. and Enzerhof M. Generalized gradient approximation made simple. *Phys. Rev. Lett.* 77:3865–8 (1996).
- S11. Monkhorst H.J., Pack J.D. Special points for Brillouin-zone integrations. *Phys. Rev. B* 13:5188–5192 (1976).

- S12 Ganguly, J., Diffusion kinetics in minerals: Principles and applications to tectono-metamorphic processes. *EMU Notes in Mineralogy*, Vol. 4 (2002), pp. 271–309.
- S13. Greenwood G. W. An analysis of the effect of multiaxial stresses and grain shape on Nabarro-Herring creep, *Phil. Mag. A*, 51:4, 537-542 (1985).
- S14. Nye, J.F. Physical Properties of Crystals. (Oxford University Press, Oxford, UK 1985) pp. 200-204.
- S15. Ford, J. M., Wheeler, J. & Movchan, A. B. Computer simulation of grain boundary creep. *Acta Materialia* 50, 3941-3955 (2002).
- S16. Wheeler, J. The preservation of seismic anisotropy in the Earth's mantle during diffusion creep. *Geophys. J. Int.* 178, 1723-1732. 2009.
- S17. Gay, N. C.. Pure shear and simple shear deformation of inhomogeneous viscous fluids .1. Theory. *Tectonophysics* 5, 211-234 (1968).
- S18. Jiang, D. A general approach for modeling the motion of rigid and deformable ellipsoids in ductile flows. *Computers & Geosciences* 38, 52-61 (2012).
- S19. Schmid, D. W. & Podladchikov, Y. Y. Analytical solutions for deformable elliptical inclusions in general shear. *Geophys. J. Int.* 155, 269-288 (2003).
- S20. Twiss, R. J. & Moores, E. M. *Structural Geology*. (W.H. Freeman, New York. 1992).
- S21. Bolioli, F., Carrez, P., Cordier, P., Devincere, B., Gouriet, K., Hirel, P., Kraych and Ritterbex, S. Pure climb creep mechanism drives flow in Earth's lower mantle. *Sci. Adv.*, 3: e1601958, (2017).
- S22. Reali, R., Van Orman, J.A., Piggott, J.S., Jackson, J.M., Bolioli, F. and Cordier, P. The role of diffusion-driven pure climb creep on the rheology of bridgmanite under lower mantle conditions. *Scientific Reports*, 9:2053, (2019).
- S23. Yamazaki, D., Kato, T., Ohtani, E. & Toriumi, M. Grain growth rates of MgSiO<sub>3</sub>- perovskite and periclase under lower mantle conditions. *Science* 274, 2052–2054 (1996).

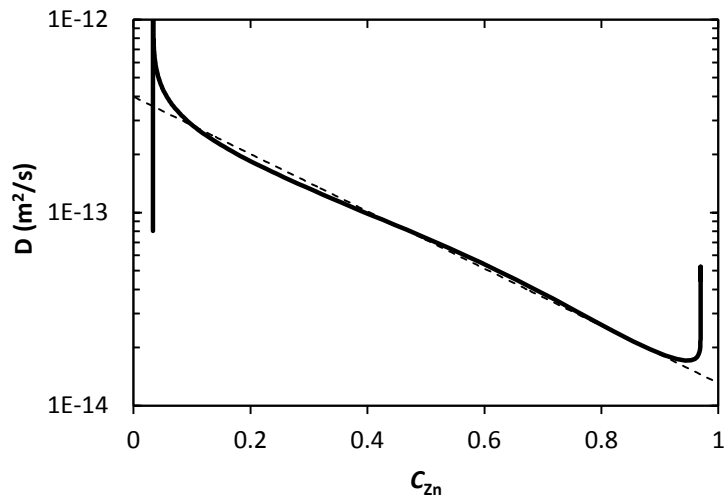
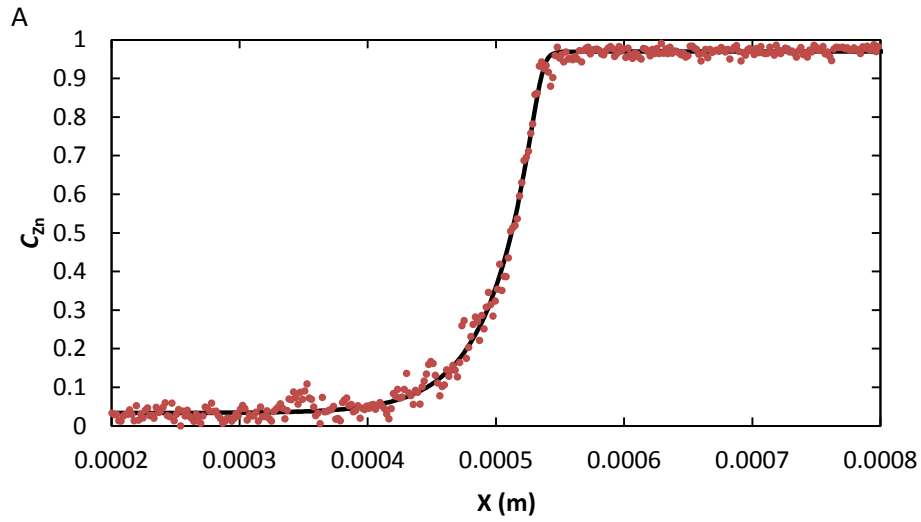


**Figure S1.** Boltzmann-Matano fit to  $NaZnF_3$ - $NaMnF_3$  perovskite interdiffusion couple run at 1.8GPa and 873 K for 90 minutes. A) Zinc concentration versus distance. The data are solid points and the sigmoidal fit is the line. B) The composition-diffusivity relationship obtained from integrating the sigmoidal fit under the Matano condition. Solid line-integral, dashed line-exponential fit.

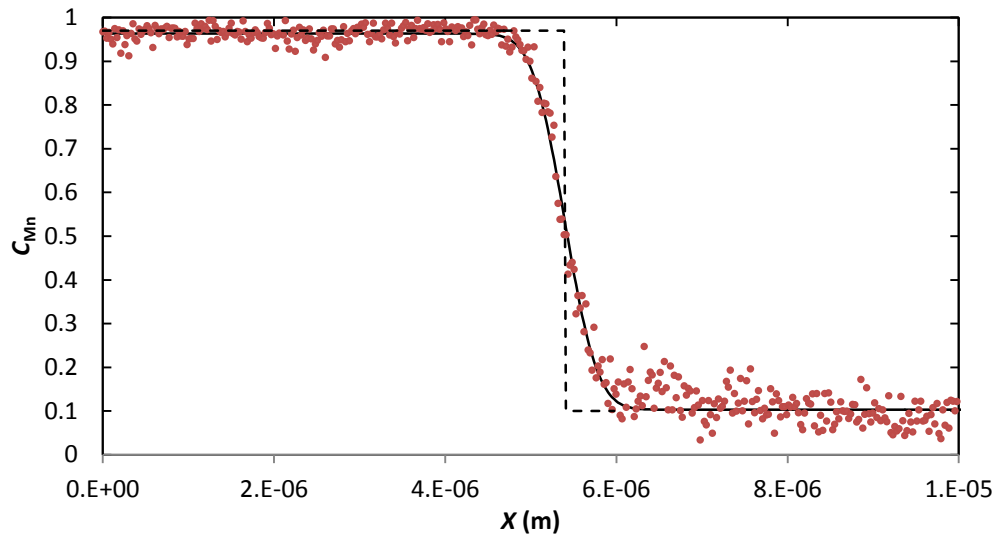


**Figure S2.** Fitted profile for couple with no diffusion to determine the convolution due to the finite beam size. The dotted line is assumed true compositional profile in this zero-second duration experiment. The solid line is this profile convolved over the best-fitting Gaussian function, with  $\sigma=0.35\mu\text{m}$ .

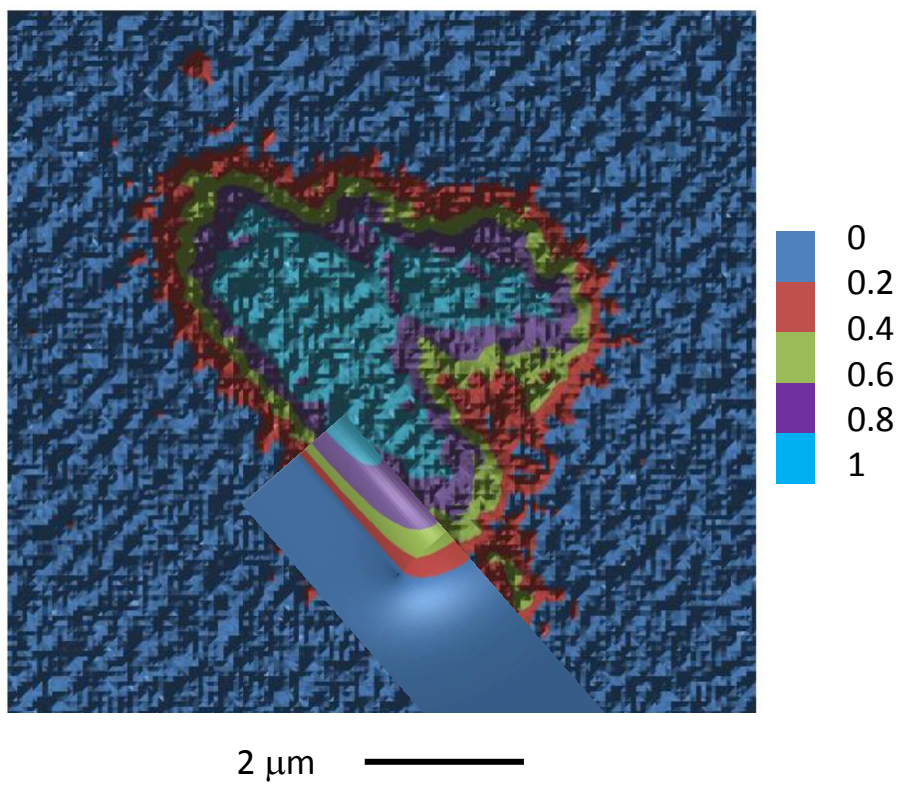


**Figure S3.** Compositional map ( $C_{Co}$ ) over a NaCoF<sub>3</sub> post-perovskite single crystal embedded in NaZnF<sub>3</sub> matrix and finite-element model of diffusion of an anisotropic cylindrical crystal in an isotropic matrix.

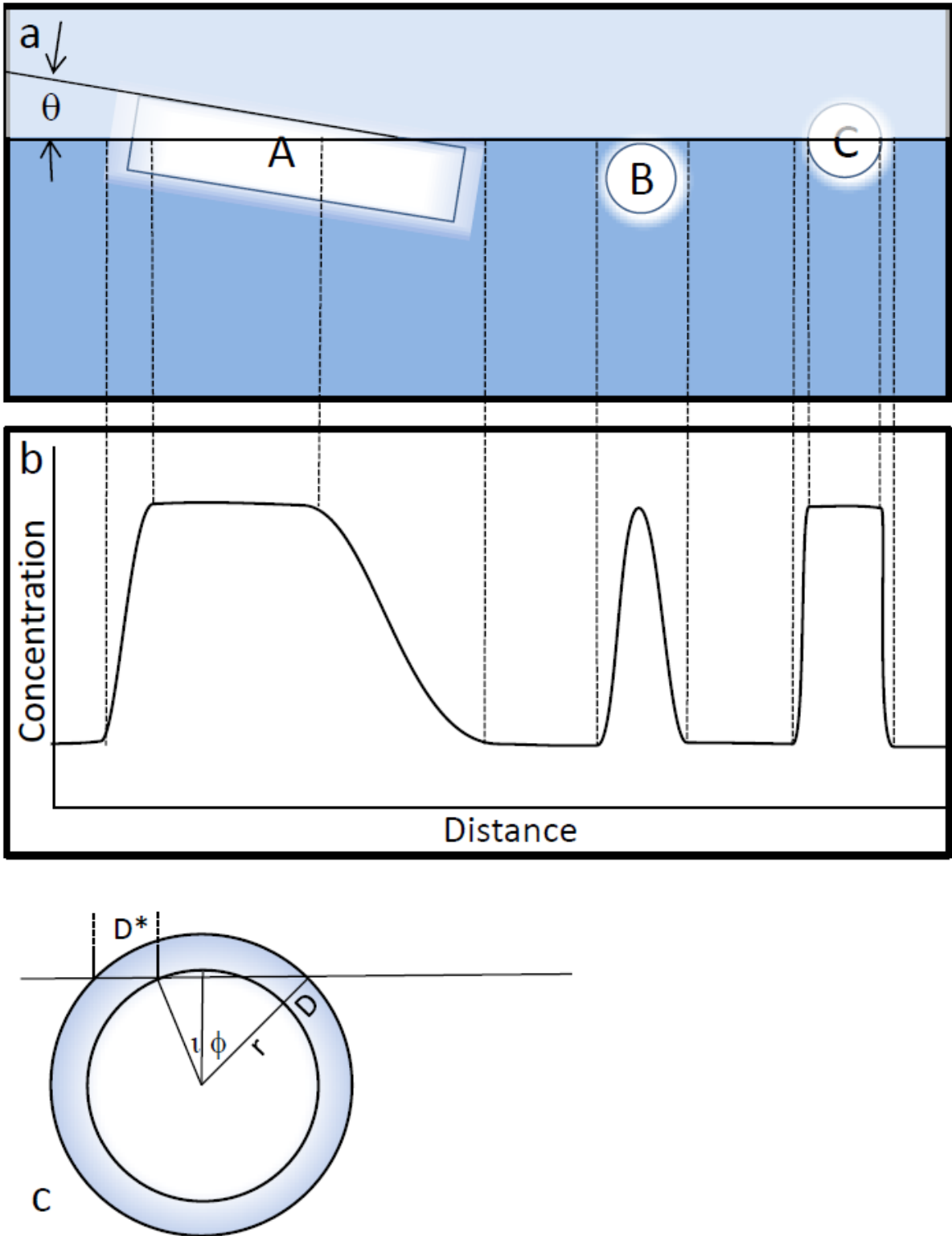


**Figure S4.** (a) Cartoon depicting 3 single crystals with isotropic chemical diffusivity intersected arbitrarily by an analytical surface and (b) the observed profiles due to these geometric convolutions. In the case of crystal A, the long axis of the crystal is not parallel to the analytical surface. Crystals B and C have long axes parallel to the analytical surface but at different depths below the surface, resulting in an apparent profile length shown diagrammatically in (c).

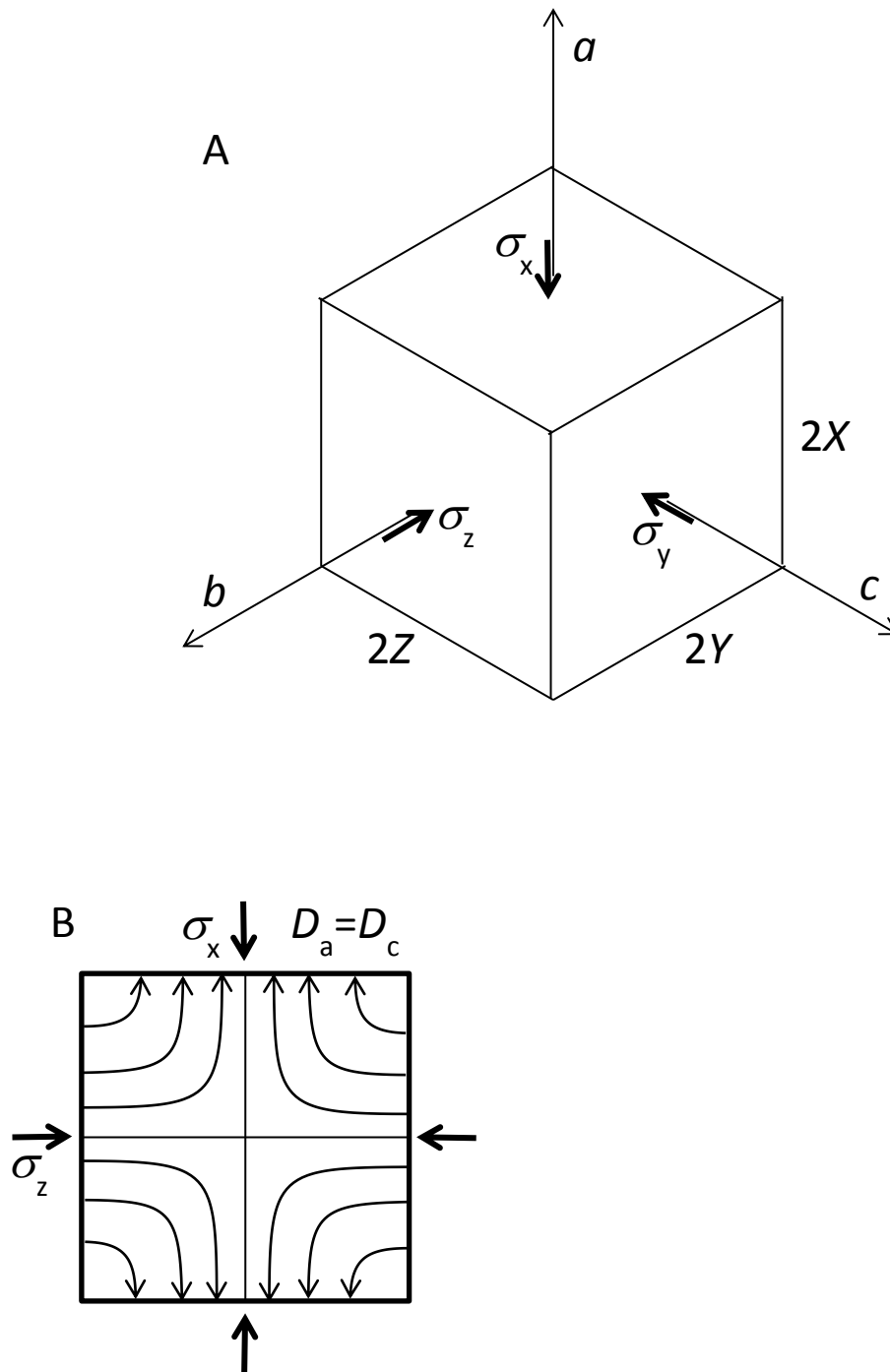
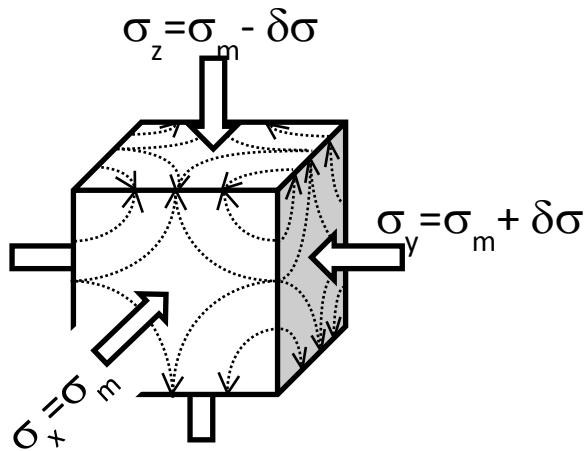


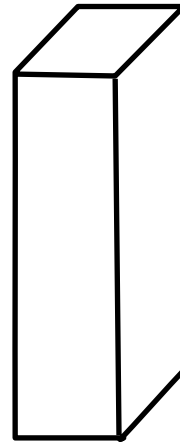
Figure S5. A: The grain geometry used in the analysis of the strain response to anisotropic chemical diffusivities. B: Vacancy flux lines in the  $a$ - $c$  plane for the case of isotropic chemical diffusivity showing that flux lines are curved and convolve diffusion in two directions for this 2-D case.

A:

Isotropic diffusivity

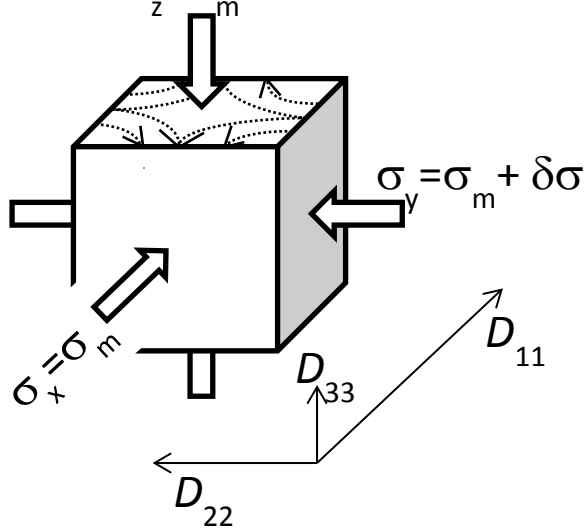


resulting shape



B:

$$D_{11} > D_{22} \gg D_{33}$$
$$\sigma_z = \sigma_m - \delta\sigma$$



resulting shape

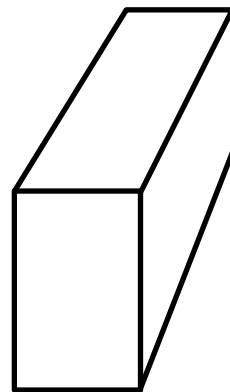


Figure S6. Strains in a crystal resulting from stresses of the form  $\sigma_x = \sigma_m$ ;  $\sigma_y = \sigma_m + \delta\sigma$ ;  $\sigma_z = \sigma_m - \delta\sigma$ . A: when the chemical diffusivity is isotropic. B: with anisotropic diffusivity of the form  $D_{11}, D_{22} \gg D_{33}$  which results in out of plane strains for the orientation of the crystal to the stress field shown here.

**Table S1.** Diffusion couples, conditions and measured diffusivity for bulk diffusion experiments.

Run #		t min	P GPa	T K	$D_{\text{Mn/Fe/Co}}$ $\text{cm}^2\text{s}^{-1}$	$D_{\text{Zn}}$ $\text{cm}^2\text{s}^{-1}$
H4017	Zn-Co	15	1.8	1043	$2.4\pm 1.8\times 10^{-13}$	$6.7\pm 2.2\times 10^{-12}$
H4018	Zn-Mn	60	1.8	973	$5.9\pm 4.1\times 10^{-12}$	$6.93\pm 0.5\times 10^{-12}$
H4038	Zn-Mn	30	1.8	1023	$1.27\pm 0.36\times 10^{-11}$	$3.69\pm 0.57\times 10^{-11}$
V879	Zn-Mn	90	1.8	873	$2.91\pm 2.0\times 10^{-13}$	$1.04\pm 0.27\times 10^{-14}$
H4053	Zn-Mn	30	6	1025	$2.38\pm 0.73\times 10^{-12}$	$1.11\pm 0.12\times 10^{-12}$
H4056	Zn-Mn	120	6	873	$1.61\pm 0.97\times 10^{-11}$	$4.04\pm 0.45\times 10^{-14}$
H4050	Zn-Mn	90	10	1023	$3.44\pm 0.42\times 10^{-12}$	$4.2\pm 1.8\times 10^{-14}$
H4042	Zn-Mn <sup>1</sup>	40	14	1073	$4.2\pm 2.1\times 10^{-12}$	$5.42\pm 2.71\times 10^{-13}$
H4066	Zn-Fe <sup>2</sup>	90	14	873	$7.31\pm 0.78\times 10^{-12}$	$1.41\pm 0.11\times 10^{-12}$
H4068	Zn-Fe <sup>2</sup>	30	14	973	$3.71\pm 0.55\times 10^{-11}$	$4.87\pm 0.73\times 10^{-12}$

**Notes:**

- 1) The sample transformed to post-perovskite during the experiment
- 2) Pre-sintered post-perovskite starting samples

**Table S2.** Diffusivity in NaCoF<sub>3</sub> post-perovskite single crystals and matrix diffusivity in NaZnF<sub>3</sub> post-perovskite from experiment at 14 GPa and 823K for 20s.

Crystal#	$D_{\text{Co fast}}$ $\text{cm}^2\text{s}^{-1}$	$D_{\text{Co slow}}$ $\text{cm}^2\text{s}^{-1}$	$D_{\text{Zn matrix}}$ $\text{cm}^2\text{s}^{-1}$
1	$5.33 \times 10^{-14}$		$2.96 \times 10^{-14}$
1	$5.25 \times 10^{-14}$		$9.59 \times 10^{-15}$
1		$2.97 \times 10^{-17}$	$1.18 \times 10^{-14}$
1		$5.44 \times 10^{-17}$	$9.99 \times 10^{-15}$
1		$1.49 \times 10^{-17}$	$2.76 \times 10^{-15}$
1		$5.75 \times 10^{-16}$	$3.19 \times 10^{-15}$
<b>Average crystal 1<sup>1</sup></b>	<b><math>5.29 \pm 0.42 \times 10^{-14}</math></b>	<b><math>6.1 \pm 3.4 \times 10^{-17}</math></b>	<b><math>4.02 \pm 0.2 \times 10^{-15}</math></b>
2	$5.17 \times 10^{-14}$		$5.87 \times 10^{-15}$
2	$6.51 \times 10^{-14}$		$8.51 \times 10^{-15}$
2		$3.90 \times 10^{-17}$	$1.15 \times 10^{-14}$
2		$4.59 \times 10^{-18}$	$7.41 \times 10^{-15}$
<b>Average crystal 2<sup>1</sup></b>	<b><math>5.80 \pm 0.6 \times 10^{-14}</math></b>	<b><math>1.33 \pm 0.74 \times 10^{-17}</math></b>	<b><math>8.1 \pm 1.0 \times 10^{-15}</math></b>

**Notes:**

Geometric averages are used here.

**Table S3.** Diffusion parameters for Na and Ni vacancy diffusion in perovskite and post-perovskite from *ab initio* simulations.

Perovskite						
$P$ (GPa)	$\Delta H_{\text{Zn}}$ (eV)	$v_{\text{Si}}$ (THz) <sup>1</sup>	$Z$	$L_{\text{Zn}}$ (Å)	$\log D_{1073}$ (m <sup>2</sup> /s)	
6-hop <sup>2</sup>						
0.01	0.82	18.62	2.00	3.75	-9.91	
1.99	0.90	18.62	2.00	3.74	-10.55	
6.00	1.01	18.62	2.00	3.69	-11.12	
15.07	1.18	18.62	2.00	3.56	-11.97	
$P$ (GPa)	$\Delta H_{\text{Na}}$ (eV)	$v_{\text{Mg}}$ (THz) <sup>1</sup>	$Z$	$L_{\text{Na}}$ (Å)	$\log D_{1073}$ (m <sup>2</sup> /s)	
<110>						
0.01	0.62	8.48	2.00	3.72	-9.31	
1.99	0.76	8.48	2.00	3.70	-10.05	
6.00	1.00	8.48	2.00	3.65	-11.21	
15.07	1.39	8.48	2.00	3.54	-13.08	
<-110>						
0.01	0.57	20.82	2.00	4.06	-8.61	
1.99	0.69	20.82	2.00	4.02	-9.24	
6.00	0.88	20.82	2.00	3.97	-10.19	
15.07	1.22	20.82	2.00	3.89	-11.77	
<001>						
0.01	0.33	22.86	2.00	3.89	-7.49	
1.99	0.69	22.86	2.00	3.86	-9.25	
6.00	0.89	22.86	2.00	3.81	-10.22	
15.07	1.21	22.86	2.00	3.78	-11.77	
Post-perovskite						
$P$ (GPa)	$\Delta H_{\text{Zn}}$ (eV)	$v_{\text{Si}}$ (THz) <sup>1</sup>	$Z$	$L_{\text{Zn}}$ (Å)	$\log D_{1073}$ (m <sup>2</sup> /s)	
<100> <sup>2</sup>						
13.92	0.61	65.84	2.00	2.78	-8.64	
20.04	0.55	65.84	2.00	2.72	-8.39	
<010>						
13.92	2.99	51.44	4.00	5.05	-19.12	
20.04	3.11	51.44	4.00	4.94	-19.70	
<001>						
13.92	1.55	61.04	2.00	3.57	-12.87	
20.04	1.67	61.04	2.00	3.51	-13.43	
6-hop <sup>2</sup>						
13.92	1.65	17.14	4.00	4.86	-13.30	
20.04	1.71	17.14	4.00	4.74	-13.65	
$P$ (GPa)	$\Delta H_{\text{Na}}$ (eV)	$v_{\text{Mg}}$ (THz) <sup>1</sup>	$Z$	$L_{\text{Na}}$ (Å)	$\log D_{1073}$ (m <sup>2</sup> /s)	
<100>						
13.92	0.64	11.22	2.00	2.71	-9.56	
20.04	0.82	11.22	2.00	2.73	-10.40	

Table S3 Continued.

$\langle 010 \rangle$						
13.92	3.18	2.31	4.00	5.05	-21.33	
20.04	3.53	2.31	4.00	4.94	-22.99	
$\langle 001 \rangle$						
13.92	1.47	8.31	4.00	3.86	-12.98	
20.04	1.66	8.31	4.00	3.85	-13.86	
$6\text{-hop}^2$						
13.92	2.26	5.54	4.00	5.28	-16.59	
20.04	2.28	5.54	4.00	5.40	-16.69	

Notes:

1. The attempt frequencies used here were calculated for for Si and Mg hopping in post-perovskite<sup>14</sup>.
2. Diffusion direction – ‘6-hop’ refers to the 6-hop cycle which is faster than direct diffusion of Zn in all directions in perovskite and along b,  $\langle 010 \rangle$ , in post-perovskite. A similar result was found<sup>14</sup> for Si diffusion in MgSiO<sub>3</sub>.

**Table S4.** Strain anisotropy produced by anisotropic diffusion creep for cases of prolate, oblate and general orthorhombic diffusion anisotropy in a cubic grain for various pure shears. The values given in the table are normalised to the slowest strain rate for each case.

	$D_{11}$	$D_{22}$	$D_{33}$	$\sigma_x$	$\sigma_y$	$\sigma_z$	$\dot{\epsilon}_x$	$\dot{\epsilon}_y$	$\dot{\epsilon}_z$
prolate	1	1	1	1	1	0	1	1	-2
	100	1	1	1	1	0	100	1	-101
	10000	1	1	1	1	0	10000	1	-10001
oblate	1	1	1	0	1	0	-1	2	-1
	1	100	100	0	1	0	-1	101	-100
	1	10000	10000	0	1	0	-1	10001	-10000
general	10000	100	1	1	0	0	101	-100	-1
	10000	100	1	0	1	0	-10000	10001	-1
	10000	100	1	0	0	1	-100	-1	101
	10000	100	1	0	1	-1	-97.06	98.06	-1
	10000	100	1	1	0	-1	50.75	-49.75	-1
	10000	100	1	1	-1	0	203.03	-202	-1